# Assimilation of *GOES-13* Imager Clear-Sky Water Vapor (6.5 $\mu$m) Radiances into a Warn-on-Forecast System

THOMAS A. JONES

*Cooperative Institute for Mesoscale Meteorological Studies, University of Oklahoma, Norman, Oklahoma*

XUGUANG WANG

*University of Oklahoma, Norman, Oklahoma*

PATRICK SKINNER

*Cooperative Institute for Mesoscale Meteorological Studies, University of Oklahoma, Norman, Oklahoma*

AARON JOHNSON AND YONGMING WANG

*University of Oklahoma, Norman, Oklahoma*

(Manuscript received 27 September 2017, in final form 23 February 2018)

ABSTRACT

A prototype convection-allowing system using the Advanced Research version of the Weather Research and Forecasting (WRF-ARW) Model and employing an ensemble Kalman filter (EnKF) data assimilation technique has been developed and used during the spring 2016 and 2017 Hazardous Weather Testbeds. This system assimilates WSR-88D reflectivity and radial velocity, geostationary satellite cloud water path (CWP) retrievals, and available surface observations over a regional domain with a 3-km horizontal resolution at 15-min intervals, with 3-km initial conditions provided by an experimental High-Resolution Rapid Refresh ensemble (HRRR-e). However, no information on upper-level thermodynamic conditions in cloud-free regions is currently assimilated, as few timely observations exist. One potential solution is to also assimilate clear-sky satellite radiances, which provide information on mid- and upper-tropospheric temperature and moisture conditions. This research assimilates *GOES-13* imager water vapor band (6.5 $\mu$m) radiances using the GSI-EnKF system to take advantage of the Community Radiative Transfer Model (CRTM) integration. Results using four cases from May 2016 showed that assimilating radiances generally had a neutral-to-positive impact on the model analysis, reducing humidity bias and/or errors at the appropriate model levels where verification observations were present. The effects on high-impact weather forecasts, as verified against forecast reflectivity and updraft helicity, were mixed. Three cases (9, 22, and 24 May) showed some improvement in skill, while the other (25 May) performed worse, despite the improved environment. This research represents the first step in designing a high-resolution ensemble data assimilation system to use *GOES-16* Advanced Baseline Imager data, which provides additional water vapor bands and increased spatial and temporal resolution.

## 1. Introduction

The short-term prediction of high-impact weather requires that accurate observations of precipitation and the surrounding synoptic environment be assimilated into numerical weather prediction (NWP) models. Reflectivity and radial velocity observations from the network of WSR-88Ds provide a wealth of data on precipitation and convection, while several statewide mesonets provide high spatial and temporal resolution surface observations. However, information about nonprecipitating clouds and the near-storm environment is also needed. Satellite observations of the atmosphere can provide this information using the sensitivity of visible, infrared, and microwave radiation to atmospheric temperature, water vapor, and cloud properties. Virtually all operational global models, such

*Corresponding author*: Dr. Thomas A. Jones, thomas.jones@noaa.gov

DOI: 10.1175/MWR-D-17-0280.1

as the Global Forecast System (GFS) and the ECMWF Integrated Forecast System, currently assimilate many types of satellite observations, mainly to characterize the cloud-free environment (e.g., Derber and Wu 1998; McNally et al. 2000, 2006). Recently, cloudy radiances have been introduced with some success, but many uncertainties remain as to how best assimilate them. Assimilating satellite observations has been shown to improve overall temperature and humidity forecasts on meso- and larger scales, but its ability to improve the forecasts of high-impact weather at a storm-scale resolution remains uncertain.

While high in information content, polar orbiting hyperspectral sensors used in operational models lack that temporal resolution and necessary low data latency required for storm-scale applications. Sensors, such as the Advanced Baseline Imager (ABI) on board the *Geostationary Operational Environmental Satellite-16* (*GOES-16*) in geostationary orbit, provide data that meet these temporal requirements but utilize far fewer channels, reducing, but not eliminating, the information content available for assimilation (Schmit et al. 2005). Despite this limitation, several studies have been conducted that assimilate geostationary orbiting imager clear- and all-sky radiances and/or retrievals and have shown that significant improvement in forecast skill is possible (e.g., Szyndel et al. 2005; Vukicevic et al. 2006; Stengel et al. 2009; Polkinghorne et al. 2010; Polkinghorne and Vukicevic 2011; Otkin 2012a,b; Qin et al. 2013; Zou et al. 2013, 2015; Jones et al. 2013a, 2014, 2015, 2016; Zhang et al. 2016). Using high-temporal-resolution data in a regional model should provide greater information content than possible on the same domain from polar-orbiting instruments, even though the latter are more likely to have a larger impact in a global model with nonfrequent temporal updates.

Several of these studies emphasize assimilating radiances over the ocean, where other observation types are sparse, to improve tropical cycle track and intensity forecasts (e.g., Zou et al. 2015; Zhang et al. 2016). For example, Zhang et al. (2016) used an ensemble Kalman filter (EnKF) approach, commonly used for radar data assimilation in convection-permitting NWP models (e.g., Aksoy et al. 2009, 2010; Dowell et al. 2011; Yussouf et al. 2013; Wheatley et al. 2015; Johnson et al. 2015), to assimilate all-sky *GOES-13* imager radiances for Hurricane Karl in the Bay of Campeche. Assimilating radiances significantly improved the characterization of the hurricane within the model while also improving track and intensity forecasts. Assessing the impact of assimilating satellite radiances over land, especially the United States, is much more challenging since other high-resolution data sources are commonly available and used in storm-scale data assimilation. Fortunately, recent research has shown that assimilating high-resolution satellite observations in combination with radar and other data sources can improve high-impact weather forecasts. Jones et al. (2013a, 2015, 2016) assimilated *GOES-13* imager cloud water path (CWP) retrievals into a rapidly cycled EnKF data assimilation system using a 3-km grid and found improvements in cloud cover, reflectivity, precipitation, and updraft helicity when assimilating these data over multiple severe weather events. As a result of these improvements, assimilating CWP has been incorporated into the real-time Warn-on-Forecast (WoF) system used by the Hazardous Weather Testbed for the spring 2016 and 2017 experiments. *GOES-16* products will be included in future experiments.

While CWP retrievals provide information on the location and thickness of clouds, they do not provide any information on the near-storm environment. On the other hand, infrared satellite radiances do provide this information since they are sensitive to atmospheric temperature and moisture at various atmospheric levels. Using an OSSE simulation, Jones et al. (2013b, 2014) showed that assimilating simulated GOES-R ABI water vapor channel radiances can improve short-term winter weather forecasts, compared to only assimilating conventional and radar observations. A similar OSSE simulation by Otkin (2012a) improved short-term precipitation forecasts for a high-impact weather event in the central United States. We focus on the water vapor–sensitive channels since atmospheric water vapor content is highly variable with few actual measurements to update the model analysis, potentially leading to large model errors (e.g., Fabry and Sun 2010). Thus, assimilating water vapor radiances provides a great opportunity for geostationary satellite data to improve high-impact weather forecasting over the United States.

The goal of this research is to assess the impact of assimilating GOES imager clear-sky water vapor radiances into a WoF system for several high-impact weather events. This research will assess the impact of assimilating radiances on the environment and how these changes affect the characteristics of forecast convection. Four high-impact weather events occurring in May 2016 are selected for study (Table 1). Each case shares similar characteristics, in that convection forms along an eastward progressing dryline in high-instability and low-inhibition environments in a relatively precipitation-free environment. Beyond these similarities, several differences exist between each case. The 9 and 24 May events (especially 24 May) were accompanied by strong dynamical forcing, whereas the 22 and 25 May events were weakly forced. Three cases also contained large areas of broken low-level clouds ahead of the dryline, with the 25 May case having significantly lower cloud coverage. Finally, the

TABLE 1. List of severe weather events for which assimilation of water vapor radiances were tested. Forecasts are initiated at 30-min intervals between 2100 and 0000 UTC for 9, 22, and 24 May and at 15-min intervals for 25 May.

| Event | Region | Forecasts |
|---|---|---|
| 9 May 2016 | Eastern OK | 2100–0000 UTC |
| 22 May 2016 | Western TX | 2100–0000 UTC |
| 24 May 2016 | Western OK, KS | 2100–0000 UTC |
| 25 May 2016 | Central KS | 2300–0030 UTC |

strong forcing associated with the 24 May event resulted in convection growing upscale into an MCS after 0000 UTC, only 2 h after convective initiation. This transition took longer in the other cases. These differences allow for a robust analysis of the effectiveness of assimilating water vapor radiances over a broad range of conditions.

Following the introduction, section 2 provides a description of GOES imager radiances and cloud property retrievals. The extended Gridpoint Statistical Interpolation analysis system (GSI)-based EnKF (GSI-EnKF) system used for the data assimilation experiments is discussed in section 3. Section 4 shows examples of assimilated observations, as well as radiance observation diagnostics. Section 5 discusses the impact of radiance data assimilation on the environmental analysis, while section 6 discusses the impact on reflectivity and rotation forecasts. Finally, section 7 provides concluding remarks.

## 2. Assimilated observations

### a. GOES Imager data

The GOES-M series imager (*GOES-12–15*) samples visible and infrared radiation from geostationary orbit over the continental United States (CONUS) at 5–15-min intervals (Menzel and Purdom 1994; Schmit et al. 2001). This instrument has five available spectral bands, including one visible (0.65 $\mu$m) and four infrared bands (3.9, 6.5, 10.7, and 13.3 $\mu$m). This research uses the band whose central wavelength is located at 6.5 $\mu$m that is primarily sensitive to mid- and upper-tropospheric moisture content in clear-sky conditions. It is also sensitive to cloud properties at similar levels during cloudy conditions. The instrument field of view at nadir is 4 km for this band. The spectral response function for the water vapor band peaks at ~375 hPa, assuming a standard atmosphere with a column relative humidity of 50% and a solar zenith angle of 50° (Fig. 1a). Sensitivity decreases toward the tropopause and nearer to the surface. The infrared band sensitive to water vapor was selected over the infrared channels since the latter are primarily sensitive to temperature, which is often well analyzed in the model analysis over a CONUS domain. Another advantage of the water vapor band is its much lower sensitivity to surface emissivity. Thus, uncertainties in the background surface emissivity table used are less of a concern for this research. Examples of *GOES-13* imager water vapor band (6.5 $\mu$m) data are shown in Fig. 2 for each event analyzed in this research. All events contain convective elements denoted by brightness temperatures ($T_{B6.5}$) < 220 K, while three out of four events contain large areas of mid- and upper-tropospheric dry air with $T_{B6.5}$ > 250 K. For 22 May, much of the clear-sky portion of the domain $T_{B6.5}$ ranges between 240 and 245 K, indicating a moister mid- to upper-tropospheric environment, compared to the other cases (Fig. 2b). The ABI on board the GOES-R (*GOES-16+*) series observes several additional spectral bands, including three sensitive to water vapor at 6.2, 6.9, and 7.3 $\mu$m (Schmit et al. 2005). The additional bands provide some information on the vertical distribution of atmospheric water vapor content and will be useful in follow-up research when *GOES-16* is fully operational (Fig. 1b).

This data assimilation system also uses cloud water path retrieved from *GOES-13* imager visible reflectances and infrared radiances using the visible infrared shortwave–infrared split-window technique (VISST), creating the SAT-CORPS product (Minnis et al. 2011). CWP and not-cloudy radiances are used since large uncertainties exist within the radiative transfer model in areas of thick clouds and precipitation. Cloud height information is also required to perform a parallax correction, which adjusts the location of high-level cirrus to their ground-relative coordinates. The impacts of assimilating CWP retrievals are described in detail by Jones et al. (2013a, 2015, 2016). CWP is also used to separate clear from cloudy pixels. All pixels where CWP > 0 kg m$^{-2}$ are considered cloudy, and corresponding radiance observations within ±1 pixel of cloudy retrievals are not assimilated. This is to reduce the potential impact of assimilating partly cloudy observations. CWP observation errors are a function of CWP value and range from 0.025 to 0.15 kg m$^{-2}$, similar to those employed by Jones et al. (2015, 2016) (Table 2).

### b. Radar and conventional data

WSR-88D Doppler radial velocity are obtained using level II data from all radars within and surrounding the regional domain for each case. Radial velocity data are dealiased and then objectively analyzed using the Observation Processing and Wind Synthesis (OPAWS) software to a 6-km horizontal grid while retaining the conical scanning surfaces (Dowell et al. 2004; Dowell and Wicker 2009). Radar reflectivity observations are derived from the Multi-Radar Multi-Sensor (MRMS) product (Smith et al. 2016), which aggregates quality-controlled reflectivity from individual radars into a fixed horizontal and

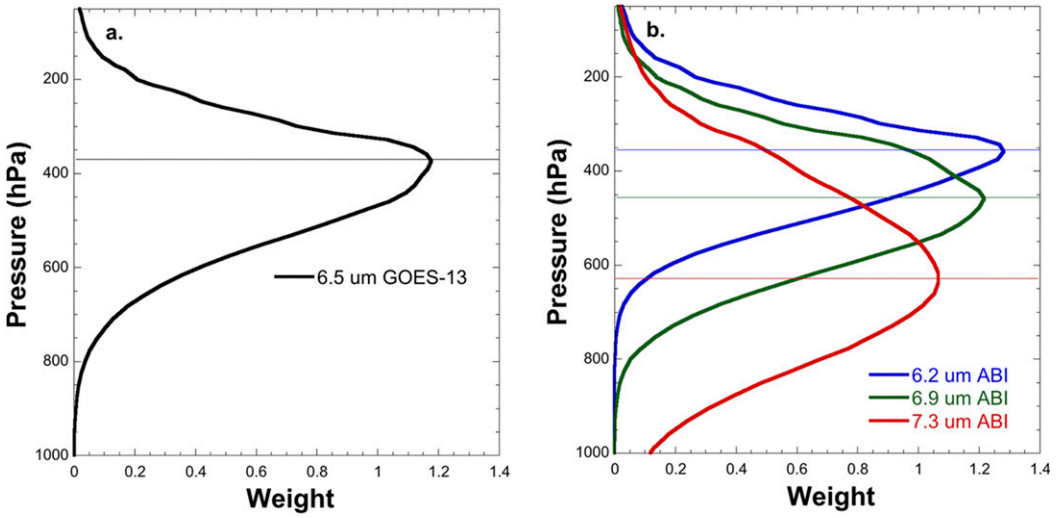


FIG. 1. Vertical weighting function for (a) *GOES-13* and (b) *GOES-16* water vapor bands, assuming a standard atmosphere with a solar zenith angle of 50° and a total column relative humidity of 50%. Horizontal lines indicate the pressure level where the weighing function peaks.

vertical grid. Observation errors for radial velocity and reflectivity are $3\,\mathrm{m\,s^{-1}}$ and $5\,\mathrm{dB}Z$, which are similar to those used by Dowell et al. (2004), Aksoy et al. (2009), and Yussouf et al. (2013) (Table 2).

All radar reflectivity and satellite observations are objectively analyzed to a 6-km grid, representing double the model horizontal resolution. Assimilating high-resolution observations such as these using the "$2\Delta x$" guideline has been shown to be optimal for assimilation into a WoF-type data assimilation system (Lu and Xu 2009). Precipitation-free (reflectivity $\leq 0\,\mathrm{dB}Z$) and clear-sky (CWP $= 0\,\mathrm{kg\,m^{-2}}$) retrievals and radiances are further thinned to 12 km by masking every other 6-km-resolution observation. Additional thinning was conducted on the clear-sky and precipitation-free areas, as it was discovered during testing that using these data at full resolution biased the model toward dry and clear conditions by incorrectly dissipating clouds and precipitation.

Finally, surface observations of temperature, pressure, humidity, and wind from the Oklahoma Mesonet are assimilated into each experiment at 15-min intervals (McPherson et al. 2007). Observation sites are confined to the state of Oklahoma, so cases centered in other regions do not assimilate this information in the current model configuration. Observation errors and covariance localization information are provided in Table 2 and are similar to those used by Wheatley et al. (2015) and Jones et al. (2016).

## 3. GSI-EnKF data assimilation system

The community GSI system represents the current standard variational data assimilation system designed for an operational environment (e.g., Kleist et al. 2009; Hu et al. 2016). The GSI contains the forward operators required to transform atmospheric observations into model state variables and includes the Community Radiative Transfer Model (CRTM; Weng 2007; Han et al. 2007), designed to specifically assimilate satellite radiances, and has recently been extended to include the necessary forward operators for radar reflectivity, Doppler radial velocity, and cloud water path (Johnson et al. 2015; Wang and Wang 2017; Jones et al. 2013a). The GSI system has been combined with an ensemble Kalman filter to take advantage of the flow-dependent covariances generated by the ensemble after each assimilation cycle (Whitaker et al. 2008). Recent studies by Johnson et al. (2015) and Wang and Wang (2017) have demonstrated the promise of using GSI-EnKF system for convective-scale radar data assimilation.

The model configuration is based on the NSSL Experimental WoF System for ensembles (NEWS-e), which represents a prototype real-time WoF system run during the 2016 and 2017 Hazardous Weather Testbeds (Stensrud et al 2009, 2013; Wheatley et al. 2015; Jones et al. 2016; Jirak et al. 2014; Gallo et al. 2017). The 2016 NEWS-e used the Advanced Research version of the Weather Research and Forecasting (WRF-ARW) Model, version 3.6.1 (Skamarock et al. 2008), coupled with the parallel ensemble adjustment Kalman filter in the Data Assimilation Research Testbed (DART) (Anderson and Collins 2007; Anderson et al. 2009) and assimilated observations at 15-min intervals into a 36-member ensemble. Initial and boundary conditions were provided by the first 18 members of an experimental 20-member

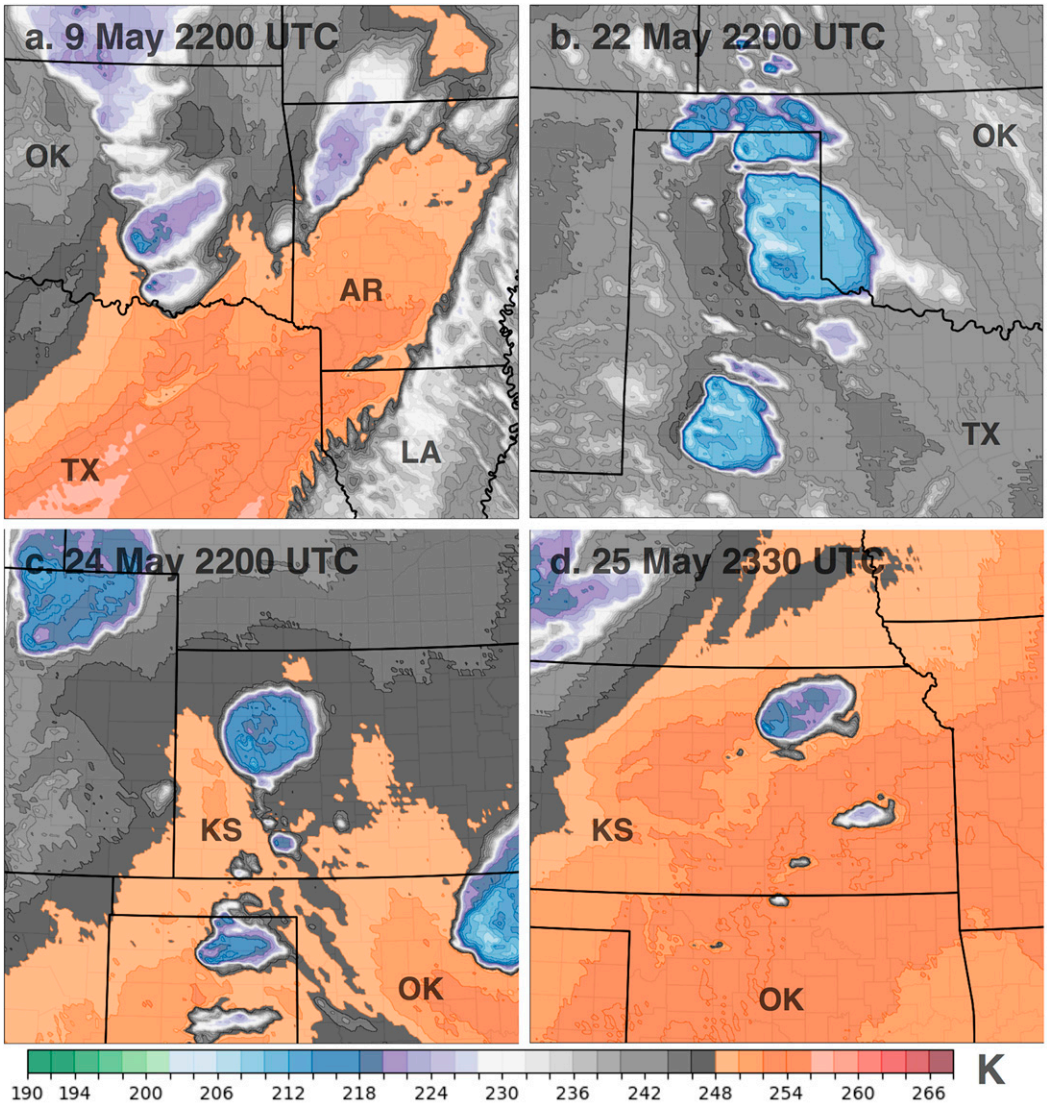


FIG. 2. *GOES-13* imager 6.5-$\mu$m water vapor band brightness temperature $T_{B6.5}$ at (a) 2200 UTC 9 May, (b) 2200 UTC 22 May, (c) 2200 UTC 24 May, and (d) 2330 UTC 25 May.

ensemble High-Resolution Rapid Refresh (HRRR-e) model (Benjamin et al. 2016). Different sets of WRF Model boundary layer physics and radiation schemes were applied to each ensemble member to introduce necessary model spread (e.g., Stensrud et al. 2000; Wheatley et al. 2014). Planetary boundary layer

TABLE 2. Observations errors and localization radii used by the GSI-EnKF system for all observation types assimilated. Errors are similar to those used by Wheatley et al. (2015) and Jones et al. (2016). Vertical localization is given in scale height (SH).

| Observation type | Error | Horizontal localization (km) | Vertical localization (SH) |
|---|---|---|---|
| Mesonet *U* wind | 1.75 m s$^{-1}$ | 60 | 0.45 |
| Mesonet *V* wind | 1.75 m s$^{-1}$ | 60 | 0.45 |
| Mesonet temperature | 1.75 K | 60 | 0.45 |
| Mesonet dewpoint | 2.0 K | 60 | 0.45 |
| Mesonet altimeter | 1.5 hPa | 60 | 0.45 |
| Reflectivity | 5.0 dB*Z* | 18 | 0.8 |
| Clear-air reflectivity | 5.0 dB*Z* | 18 | 0.8 |
| Radial velocity | 3.0 m s$^{-1}$ | 18 | 0.8 |
| CWP | 0.025–0.15 kg m$^{-2}$ | 36 | 1.0 |
| Clear-sky 6.5-$\mu$m $T_B$ | 1.5 K | 36 | 4.0 |

(PBL) schemes include Yonsei University (YSU), Mellor–Yamada–Janjić (MYJ), and Mellor–Yamada–Nakanishi–Niino (MYNN; Hong et al. 2006; Janjić 1994; Nakanishi and Niino 2006). Radiation schemes include the Rapid Radiative Transfer Model (RRTM), RRTM for general circulation models (RRTMG) for both shortwave and longwave radiation, and Dudhia scheme for shortwave radiation only (Mlawer et al. 1997; Iacono et al. 2008; Dudhia 1989). Table 3 indicates the combination of PBL and radiation schemes used for each member, which is similar to the configuration described in Wheatley et al. (2015). To create the 36 members needed for the data assimilation system, the same physics diversity is applied to the reverse order of HRRR-e members so that NEWS-e member 19 is based on the physics combination used in member 1, but the initial conditions from HRRR-e member 18 (Table 3). The NEWS-e system initialized at 1800 UTC, using 1-h forecasts generated from the members of the HRRR-e at 1700 UTC. The horizontal resolution for both is 3 km, with 51 vertical levels from the surface to 10 hPa over a 250 × 250 gridpoint domain, which results in a domain size of 750 km × 750 km. The location of each domain was selected to capture the primary severe weather event of the day, and during real-time testing, the center point is based on Storm Prediction Center (SPC) outlook guidance. All ensemble members utilized radiation-aware Thompson cloud microphysics (Thompson et al. 2004, 2008), and no cumulus parameterization was applied. No covariance inflation is applied to the system, though additive noise is applied to temperature, humidity, and wind where reflectivity observations are >25 dB$Z$ (Dowell and Wicker 2009). The primary difference between the NEWS-e and the system used in this research is the replacement of DART with the GSI-EnKF system to utilize the CRTM integration present within GSI, enabling the direct assimilation of satellite radiances.

TABLE 3. PBL and radiation scheme options contained within each 2016 configuration NEWS-e member. HRRR-e member indicates the HRRR-e member from which the initial conditions used in the corresponding NEWS-e member originate. Adapted from Table 2 in Wheatley et al. (2015).

| HRRR-e member | NEWS-e member | PBL | Radiation | |
|---|---|---|---|---|
| | | | SW | LW |
| 1 | 1 | YSU | Dudhia | RRTM |
| 2 | 2 | YSU | RRTMG | RRTMG |
| 3 | 3 | MYJ | Dudhia | RRTM |
| 4 | 4 | MYJ | RRTMG | RRTMG |
| 5 | 5 | MYNN | Dudhia | RRTM |
| 6 | 6 | MYNN | RRTMG | RRTMG |
| 7 | 7 | YSU | Dudhia | RRTM |
| 8 | 8 | YSU | RRTMG | RRTMG |
| 9 | 9 | MYJ | Dudhia | RRTM |
| 10 | 10 | MYJ | RRTMG | RRTMG |
| 11 | 11 | MYNN | Dudhia | RRTM |
| 12 | 12 | MYNN | RRTMG | RRTMG |
| 13 | 13 | YSU | Dudhia | RRTM |
| 14 | 14 | YSU | RRTMG | RRTMG |
| 15 | 15 | MYJ | Dudhia | RRTM |
| 16 | 16 | MYJ | RRTMG | RRTMG |
| 17 | 17 | MYNN | Dudhia | RRTM |
| 18 | 18 | MYNN | RRTMG | RRTMG |
| 18 | 19 | YSU | Dudhia | RRTM |
| 17 | 20 | YSU | RRTMG | RRTMG |
| 16 | 21 | MYJ | Dudhia | RRTM |
| 15 | 22 | MYJ | RRTMG | RRTMG |
| 14 | 23 | MYNN | Dudhia | RRTM |
| 13 | 24 | MYNN | RRTMG | RRTMG |
| 12 | 25 | YSU | Dudhia | RRTM |
| 11 | 26 | YSU | RRTMG | RRTMG |
| 10 | 27 | MYJ | Dudhia | RRTM |
| 9 | 28 | MYJ | RRTMG | RRTMG |
| 8 | 29 | MYNN | Dudhia | RRTM |
| 7 | 30 | MYNN | RRTMG | RRTMG |
| 6 | 31 | YSU | Dudhia | RRTM |
| 5 | 32 | YSU | RRTMG | RRTMG |
| 4 | 33 | MYJ | Dudhia | RRTM |
| 3 | 34 | MYJ | RRTMG | RRTMG |
| 2 | 35 | MYNN | Dudhia | RRTM |
| 1 | 36 | MYNN | RRTMG | RRTMG |

The observation error for clear-sky $T_{B6.5}$ was set to 1.5 K, similar to the default value present in the GSI "satinfo" file (1.4 K). The horizontal localization radius following Gaspari and Cohn (1999) was set to 36 km, which is the same used for the CWP retrievals currently used in this data assimilation system. Assigning a vertical localization radiance is more challenging since a cloud-free radiance observation has no specific height value to use as a vertical coordinate. The atmospheric level where the sensitivity is greatest is a function of temperature, humidity, cloud cover, and trace gas concentration. This value is a function of atmospheric conditions, time of day, and model resolution. For this research, the level of the maximum Jacobian of $T_{B6.5}$ at each observation point is assigned as the vertical pressure height and is calculated from the analysis background of each ensemble member at each assimilation cycle. Vertical localization is set to 4.0 in units of scale height, which corresponds to a very large, but not quite infinite, radius of influence. Even though the vertical localization is very large, some sensitivity to the assigned vertical level of the observation remains. There remains significant uncertainty in the ideal vertical pressure height and localization to apply to radiances in ensemble data assimilation systems (e.g., Lei et al. 2016), and those used here represent values that performed well after several sensitivity tests were undertaken.

To properly assimilate clear-sky radiances, a bias adjustment must be applied to account for both observation biases and biases in the radiative transfer model

(e.g., Derber and Wu 1998; Harris and Kelly 2001; Auligné and McNally 2007; Auligné et al. 2007; Dee and Uppala 2009; Ren 2016). Otherwise, the resulting model update would have a significant dry or moist bias. Fortunately, the GSI system has built in tools to apply bias correction to a multitude of sensors and bands, including GOES imager water vapor radiances. The operational bias adjustment scheme is a function of the global bias, zenith angle, cloud liquid water, and temperature lapse rate, which represents the overall airmass component (Derber and Wu 1998; Wu et al. 2002; Zhu et al. 2014). Additionally, there is a scan angle component that was applied separately (Derber and Wu 1998). The most recent iteration of the bias adjustment scheme is used here, where the airmass-dependent and angle-dependent components are combined into a single function (Zhu et al. 2014). Since the bias adjustment coefficients are likely to change as a function of time due to changes in the environment, the bias adjustment is updated at each assimilation cycle. For this research, the bias adjustment is applied in two steps. First, a constant 2.75 K bias adjustment is applied during the computation of model priors. If no bias adjustment is applied at this step, the quality-control algorithms often discard large amounts of good data. The remaining portion of the bias adjustment is applied during the data assimilation step using the Zhu et al. (2014) method and is updated after each assimilation cycle. The total magnitude of the bias adjustment for these events generally ranges between 3.25 and 4.0 K.

In addition to clear-sky water vapor satellite radiances, this system assimilates WSR-88D radial velocity and reflectivity observations, *GOES-13* satellite cloud water path retrievals (Minnis et al. 2011; Jones et al. 2015), and Oklahoma Mesonet data, resulting in one of the first systems that combines radiances with these other high-resolution observation types. Table 1 provides a list of assimilated observations, along with their observation errors and localization radii. All available observations are assimilated at 15-min intervals continuously from 1800 to 0000 or 0030 UTC the next day, depending on data availability. Assimilation of CWP ceases at sunset due to greater uncertainties present with the nighttime retrieval algorithm. For these cases, this generally occurs around 0000 UTC. Two-hour forecasts are generated for up to seven analysis times from the first 18 members of the ensemble, corresponding to the period of severe weather during a particular event, with forecasts output at 5-min intervals (Table 2). Using the first 18 members captures the full physics diversity of the ensemble while reducing the required computing resources. Two sets of experiments are performed. The first assimilates Oklahoma Mesonet, radar reflectivity and radial velocity, and CWP retrievals, which is labeled as control (CNTL), while the second adds clear-sky $T_{B6.5}$ to the set of observations assimilated and is labeled the water vapor (WV) experiment. Analyses and forecasts from each set of experiments are compared to determine the impact of assimilating $T_{B6.5}$ on the environment and supercell storm forecasts.

## 4. Observation diagnostics

Figure 3 shows assimilated surface, radar, and satellite observations at a selected time for each case studied. Large areas of clear-air reflectivity (0 dB$Z$) are being assimilated in the precipitation-free areas within each domain with reflectivity (>20 dB$Z$) and radial velocity being assimilated where precipitation is present (Figs. 3a,d,g,j). For 24 May, only a few reflectivity observations are being assimilated at 2200 UTC, as convection is still developing and not yet analyzed by the model; thus, they are being thrown out as outliers (Fig. 3g). A large number of satellite observations are also being assimilated for each case (Figs. 3b,e,h,k). In clear-sky areas, both CWP = 0 and $T_{B6.5}$ are being assimilated, whereas in cloudy areas, CWP > 0 observations are assimilated. Note that 9 and 22 May contain large areas of both convective and nonconvective clouds, limiting the potential impact of assimilating $T_{B6.5}$ (Figs. 3b,e). The number of $T_{B6.5}$ observations assimilated per cycle is fewer than 1000 for 9 May and between 1500 and 2000 for 22 May (Fig. 4). Conversely, the 24 and 25 May events contain larger clear-sky regions and assimilate many more observations per cycle (Figs. 3h,k, 4). Satellite observations were not available at 1800, 2100, and 0000 UTC since the *GOES-13* imager switches to global mode at 3-h intervals, eliminating the CONUS files used for processing.

To determine where the greatest impact from assimilated $T_{B6.5}$ for each case should be expected, the assigned vertical pressure height from the CRTM for each $T_{B6.5}$ observation is shown in Figs. 3c, 3f, 3i, and 3l. This pressure height is essentially the level at which the peak of the weighting function (Fig. 1) exists for the model environment at the observation location. The vertical height varies from ~500 hPa in parts of Kansas on 25 May to nearly 250 hPa on 22 May. One consistent pattern from all the cases is that the vertical level is lower in drier conditions. Where the vertical pressure height >450 hPa, $T_{B6.5}$ often exceeds 250 K (Figs. 2, 3). The 22 May event differed from the other cases in having a moister environment, resulting in the vertical coordinate being higher in the atmosphere for this case. As a result, the effects of assimilating these data will vary depending on case and location and be maximized in different atmospheric layers. In some cases, the

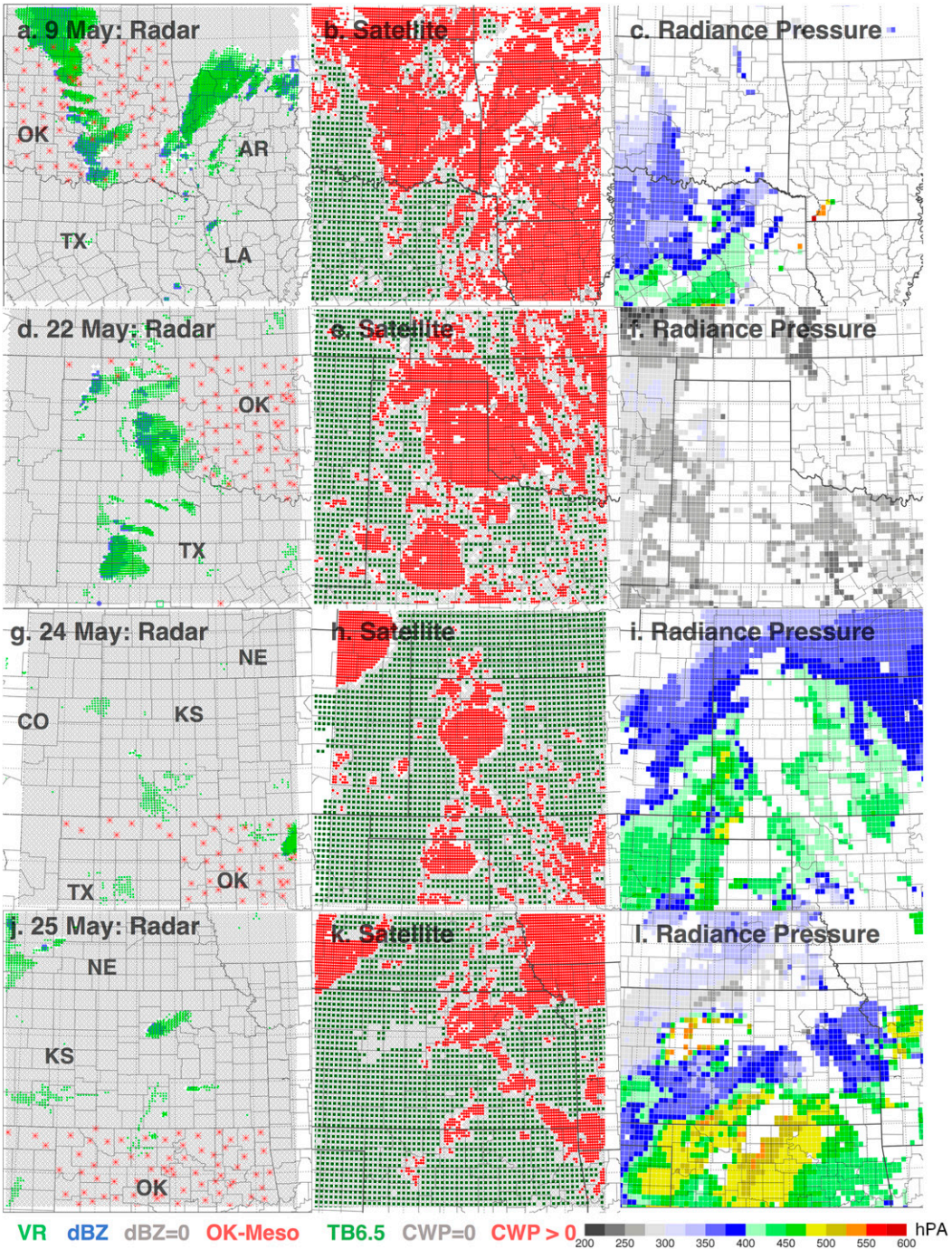


FIG. 3. Assimilated observations for each event. (a),(d),(g),(j) Radar radial velocity, reflectivity, and Oklahoma Mesonet observation locations at the times shown in Fig. 2. (b),(e),(h),(k) Corresponding satellite observations (CWP and $T_{B6.5}$) assimilated at the same time. Outliers are not plotted. (c),(f),(i),(l) The vertical height assigned to each $T_{B6.5}$ observation by the CRTM.

impact will be maximized above 300 hPa (22 May) and in others, near or below 500 hPa (25 May).

The overall impact of assimilating $T_{B6.5}$ can be determined by calculating the innovation (e.g., bias), root-mean-square innovation (RMSI), and total spread (TSPRD) during each assimilation cycle (Dowell et al. 2004; Dowell and Wicker 2009; Dowell et al. 2011; Yussouf et al. 2013; Wheatley et al. 2015; Jones et al.

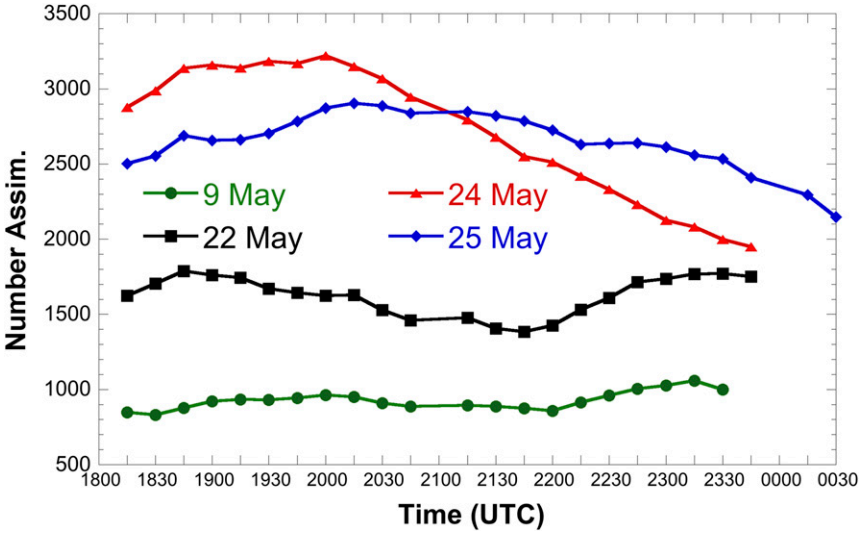


FIG. 4. Number of assimilated $T_{B6.5}$ clear-sky observations as a function of time for each case. No data were available at 1800, 2100, and 0000 UTC.

2016). Details and equations for these observation diagnostics are provided by the previous references and are also briefly defined below, based on the discussion provided in Jones et al. (2016). The difference between prior and posterior fields and observations represents the innovation, and RMSI is the corresponding error between observations and model analyzed variables. Ensemble spread is the average innovation between the individual ensemble forecasts of an observation type, such as $T_{B6.5}$ or reflectivity, and the ensemble mean forecast. The summation of the prior ensemble variance and the observation error variance results in TSPRD, and consistency ratio (CR) is the ratio of prior ensemble variance ($RMSI^2$) to the square of TSPRD. When CR is near 1.0, the ensemble variance is an optimal approximation of the error variance for a corresponding observation error (Dowell et al. 2004; Aksoy et al. 2009; Dowell and Wicker 2009). When CR $<$ 1.0, the ensemble contains insufficient spread, while CR $>$ 1.0 indicates an ensemble with excessive spread.

Innovation, RMSI, TSPRD, and CR for clear-sky-only $T_{B6.5}$ are shown for each case in Fig. 5. Statistics for radial velocity, radar reflectivity, and CWP are all consistent with those shown in previous research and will not be discussed here (e.g., Yussouf et al. 2013; Wheatley et al. 2015; Jones et al. 2016). The prior innovation represents the innovation applied at the beginning of the ensemble data assimilation step before the flow-dependent bias adjustment is applied, but after the constant bias adjustment has been applied during the GSI step. Prior innovation ranges between 0.25 and 1.25 K at early analysis times and generally remains in that range for the duration of the cycling out to 0000 UTC. For 9 and 22 May, prior innovation changes as a function of time, decreasing for 9 May and increasing for 22 May as atmospheric conditions evolve for these cases (Figs. 5a,b). In both cases, the amount of cloud cover increases, and the number of assimilated observations decreases. Posterior innovation is generally less than $\pm$0.25 K for all cases. RMSI generally ranges between 0.5 and 1.5 K, with the posterior value being $\sim$0.5 K less than the prior value, indicating an overall reduction in $T_{B6.5}$ error during each assimilation cycle. TSPRD is roughly constant at $\sim$1.6 K for all cases after the first two assimilation cycles. The overall CR differs from case to case but is $>$1 for most assimilation cycles. Experiments using a smaller observation error (1.25 K) to lower spread did result in a more ideal CR for all cases in the early assimilation periods, but also generated significant overfitting problems in later periods (not shown). Also, CR decreases as a function of time for two cases (22 and 24 May), falling below 1 by 2300 UTC (Figs. 5b,c). For 22 May, the number of assimilated observations behind the dryline increases, while the number ahead decreases. Behind the dryline, simulated clear-sky $T_{B6.5}$ are relatively homogeneous, reducing overall spread at later forecast times. Similar behavior occurred on 24 May, as the rapid growth of the convective clouds reduced assimilated observations in the prestorm environment, leaving only those in the less-perturbed area behind the dryline. Overall, the saw-tooth pattern of innovation and RMSI indicate that the assimilation of clear-sky $T_{B6.5}$ is successful at reducing simulated $T_{B6.5}$ model errors, and now it is important to determine if this

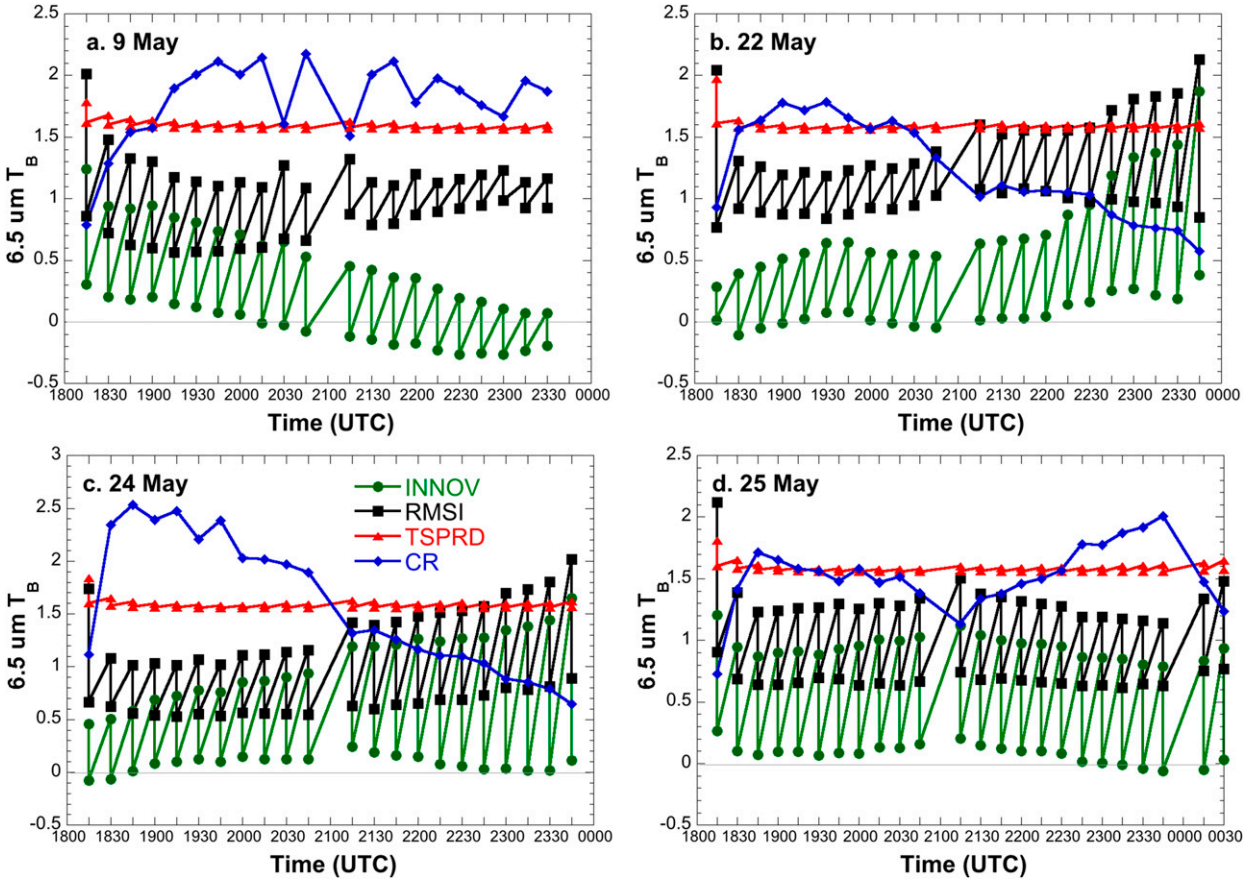


FIG. 5. Innovation, RMSI, TSPRD, and CR (unitless) for each case.

reduction in error corresponds to an improvement in the analyzed atmospheric conditions.

## 5. Environmental impact

The impact of assimilating $T_{B6.5}$ can be assessed in several ways. First, the simulated ensemble mean $T_{B6.5}$ from both experiments are compared at selected analysis times, corresponding to observations in Fig. 2 (Fig. 6). For all cases, simulated $T_{B6.5}$ are generally lower than the corresponding observations, which requires the application of the bias adjustment described in section 3. However, assimilating $T_{B6.5}$ still has a significant impact on the model analysis, with differences of up to 5 K present in clear-sky regions (Fig. 6l). Differences in cloudy areas, defined as when either CNTL or WV indicates clouds, are masked out, as they can vary significantly due to relatively minor differences in the microphysical properties of the clouds.

At 2200 UTC 9 May, WV generates lower $T_{B6.5}$ in much of central and northern Texas, with a narrow band of increased $T_{B6.5}$ located to the southeast of convection in southern Oklahoma (Figs. 6a–c). Smaller differences are present in central Oklahoma behind the dryline. At 2200 UTC 22 May, several areas where $T_{B6.5}$ differs between CNTL and WV are present, with the most apparent occurring in the clear-sky areas west of the ongoing convection and another area in central Texas, east of the convection. In the latter area, $T_{B6.5}$ is reduced on the order of 1–2 K, except in a small pocket, where an increase of ~1 K occurs (Figs. 6d–f). Similar differences are apparent on at 2200 UTC 24 May, with $T_{B6.5}$ decreasing 1–2 K east of developing convection in Kansas and Oklahoma (Figs. 6g–i). The greatest differences between CNTL and WV are reserved for the 25 May event, where $T_{B6.5}$ increases up to 5 K in central Kansas and 2–3 K over much of the state, surrounding the convection located in north-central Kansas at this time (Figs. 6j–l). The $T_{B6.5}$ *GOES-13* image in Fig. 2d indicates a very dry mid- to upper-level environment, and the difference between CNTL and WV suggests that CNTL may have a significant moist bias, which will be explored in greater detail below.

The differences between CNTL and WV experiments are generally consistent with the difference between

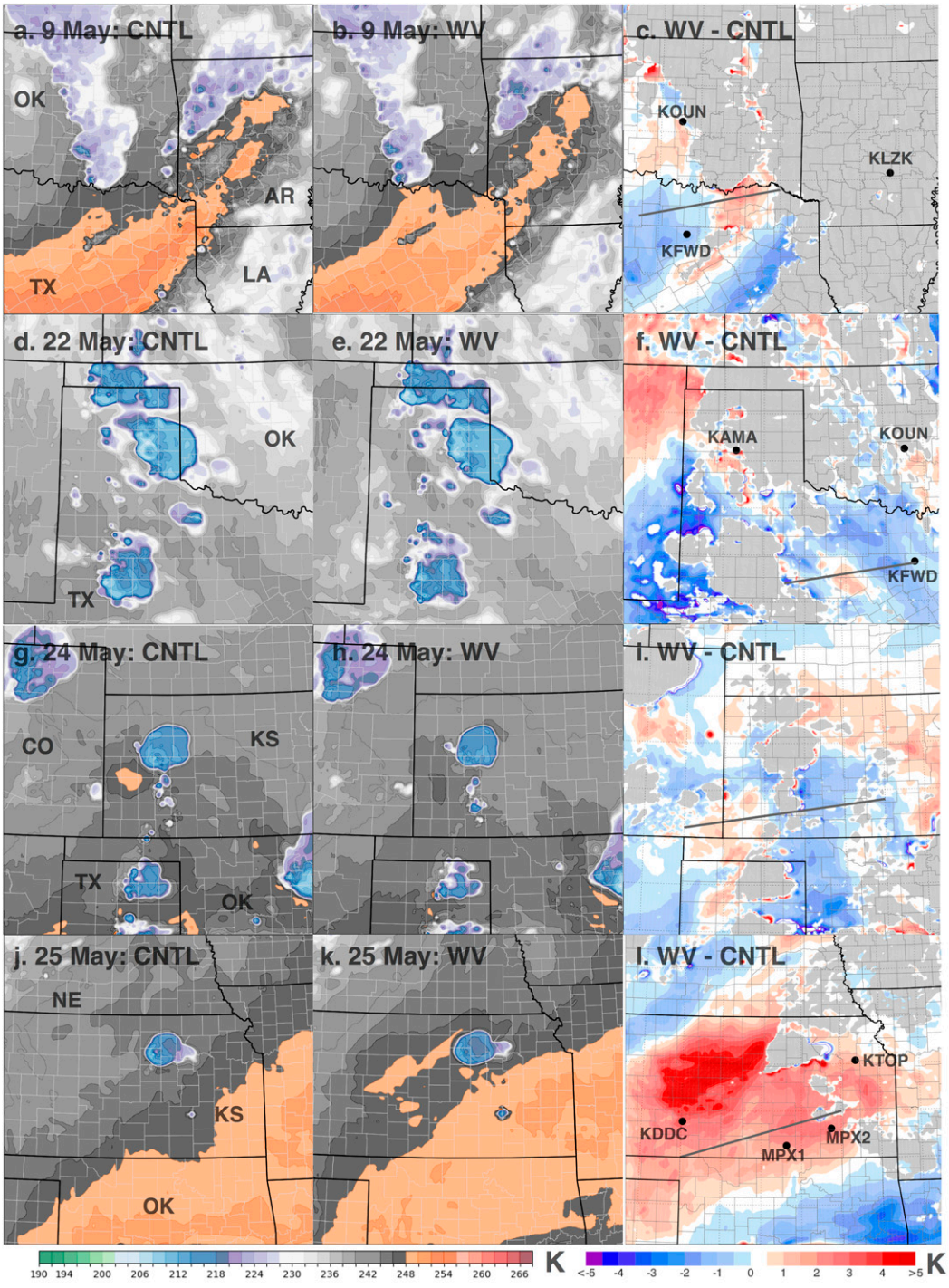


FIG. 6. Synthetic $T_{B6.5}$ for (a),(d),(g),(j) CNTL and (b),(e),(h),(k) WV experiments at 2200 UTC 9, 22, and 24 May and 2330 UTC 25 May. (c),(f),(i),(l) Difference in $T_{B6.5}$ (WV − CNTL) for each case. Lines indicate the location of dewpoint cross sections shown in Fig. 8, and black dots indicate the locations of soundings present within the domain of each case, which are shown in Figs. 9–11.

bias-adjusted observations and the ensemble mean WV model analyses at these times ($O - A$; Fig. 7). Note that observations have been bias adjusted prior to calculating these differences. In most cases, where observations are warmer than the prior forecasts, the difference between CNTL and WV is also positive. The same is true for

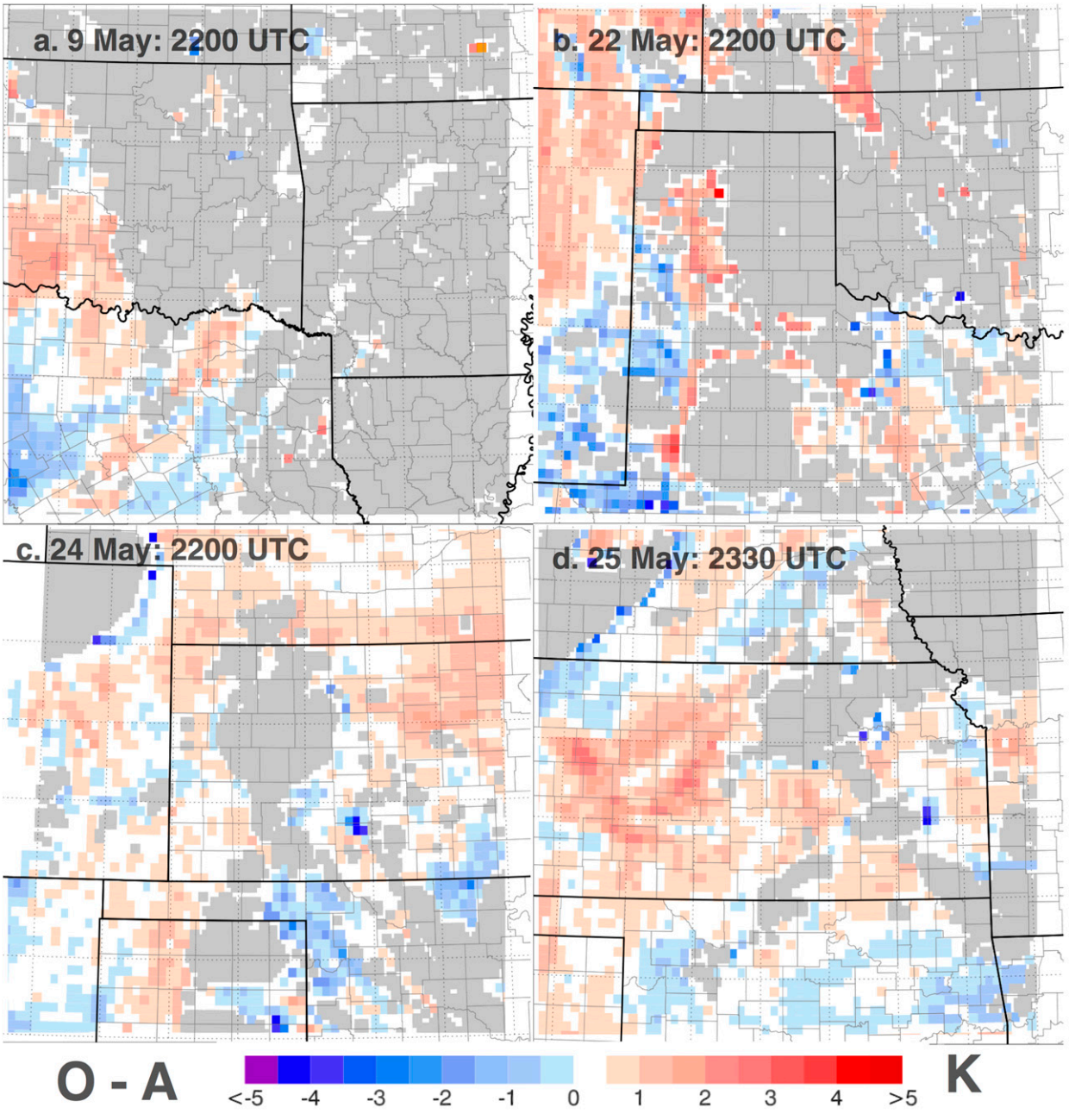


FIG. 7. Difference in ensemble mean simulated $T_{B6.5}$ from WV and *GOES-13* $T_{B6.5}$ ($O - A$) for each case at 2200 UTC 9, 22, and 24 May and 2330 UTC 25 May.

negative differences. Some exceptions do exist, and the magnitudes of the model differences are generally greater. However, the model differences have the advantage of 4–6 h of data assimilation, while the $O - A$ plots only represent the differences at a single time.

The differences in observed and simulated $T_{B6.5}$ should correspond to differences in the model environment, especially in relation to atmospheric moisture content. To measure these differences, west to east cross sections of dewpoint were created at the locations and analysis times denoted in Fig. 6 for each case. Dewpoint is plotted instead of water vapor mixing ratio so that differences can be visualized at all levels using a linear scale. Figure 8 shows the dewpoint differences (WV − CNTL) along these cross sections and the $T_{B6.5}$ difference along the same track. For all cases, positive $T_{B6.5}$

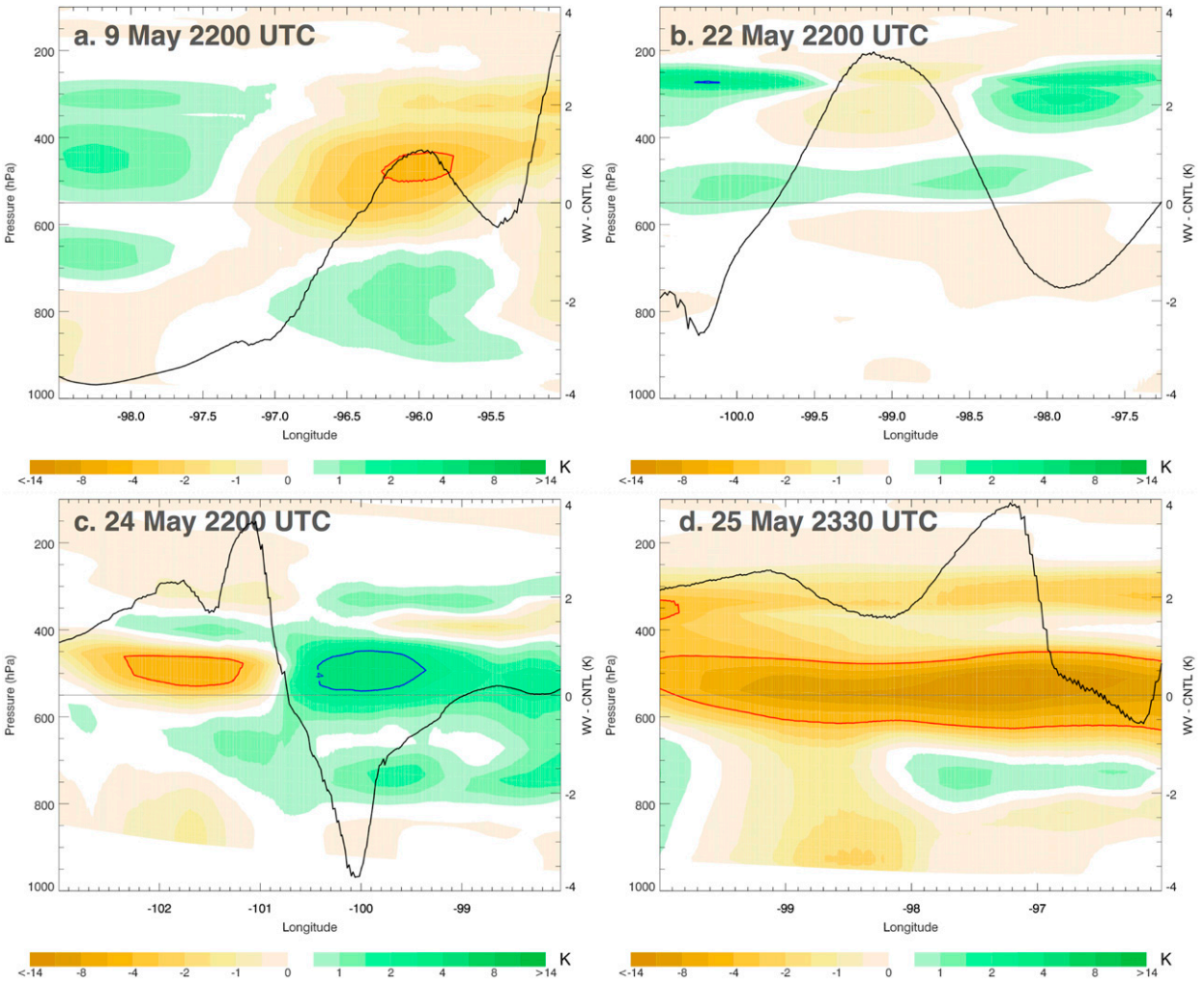


FIG. 8. West–east vertical cross sections of dewpoint difference (WV − CNTL) for each event at the times shown in Fig. 6. Red contours indicated a dewpoint innovation of <4 K, and blue contours indicate dewpoint innovation >4 K. The difference in simulated $T_{B6.5}$ along the same track is represented by the black line.

differences generally correspond to a decrease in dewpoint above 600 hPa. This is consistent with higher $T_{B6.5}$ being associated with drier atmospheric conditions. Conversely, dewpoint increases when the $T_{B6.5}$ difference is negative. The magnitude and location of these differences change from case to case. On 9 May, the largest differences occur between 550 and 400 hPa, with smaller differences above and below (Fig. 8a). Near 96.0°W, the decrease in dewpoint exceeds 4 K in a small area, with a much larger area of decreases >1 K surrounding this location. Below 650 hPa, a dewpoint increases slightly (<1 K) in the same area. The region east of 96.5°W represents the environment that is entrained into the southern Oklahoma convection over the next 2 h, and its impact on forecast convection is explored further in section 6.

The dewpoint differences along the selected cross section on 22 May are the smallest of all the experiments and are also maximized at the highest altitude (~300 hPa), which is consistent with the higher vertical coordinates assigned to the $T_{B6.5}$ observations for this event (Fig. 3f). The cross section transverses the area in central Texas, where both a decrease and increase in $T_{B6.5}$ were observed (Fig. 8b). Thus, the upper-level environment east of the ongoing convection shows both increases and decreases in moisture, depending on location. Larger differences are apparent on 24 May (Fig. 8c). On this day, a dryline is located along the 101°W parallel with convection developing on the eastern side. The cross section transverses the dryline, with WV being drier in the 550–450-hPa layer in excess of 4 K while increasing moisture to the east. These changes are consistent with the positive to negative $T_{B6.5}$ difference along this track. The largest dewpoint differences occur for the 25 May event, with WV being in excess of 4 K

drier between 600 and 450 hPa along the entire track located across southern Kansas (Fig. 8d). A secondary layer of drying occurs near 350 hPa. Given the large difference between observed and simulated $T_{B6.5}$, the large impact to the model environment is expected.

Finally, it is important to determine if changes in the model environment from assimilating $T_{B6.5}$ are consistent with observed atmospheric conditions. Unfortunately, high spatial and temporal resolution upper-air observations of moisture are not readily available, preventing a complete verification. However, some aircraft, operational soundings, and experimental soundings from the Mesoscale Predictability Experiment (MPEX) are available, allowing a few snapshot comparisons of the model environment to reality. Significant limitations exist, with these comparisons due to poor spatial and temporal sampling and the potential observations to be strongly impacted by cloud cover. The criteria for using observed soundings are that they occur between 2100 and 0000 UTC and are not near the boundary of the domain. For the 9 May case, three operational soundings from 0000 UTC (10 May) exist within the model domain. They are located in Fort Worth, Texas (KFWD), Norman, Oklahoma (KOUN), and Little Rock, Arkansas (KLZK), each sampling different conditions (Fig. 9). The location of each sounding is given in Fig. 6. Ensemble mean profiles of temperature and dewpoint at 0000 UTC are compared with the observations at each site (Fig. 9). At KFWD, WV moistens the 400–450-hPa layer, better matching observations, but this moistening carries over into a dry layer observed in the 450–525-hPa layer (Fig. 9a). The boundary layer moisture at KFWD is overestimated by both experiments. At KOUN, differences between CNTL and WV are small, with the latter having a slightly better match to observations in the 350–450-hPa layer (Fig. 9b). Unlike the KFWD location, the boundary layer is almost perfectly analyzed by both experiments. Both KFWD and KOUN represent conditions behind the dryline in the post-convection environment. The third sounding at KLZK is located ahead of the dryline, but there is ongoing precipitation at this site at the time of the sounding. The sounding and model analyses indicated a saturated atmosphere from just above the surface to 650 hPa (Fig. 9c). Above this layer, differences in CNTL and WV exist, but it is difficult to discern which is better or worse. The overall dewpoint error is given in Table 4, with WV generating a larger overall error at KFWD, a slightly smaller error at KOUN, and similar errors at KLZK. Differences in temperature between CNTL and WV are small for all sites for this and all later cases.

Three operational soundings were also available within the domain for the 22 May case, including sites at Amarillo (KAMA), KFWD, and KOUN (Fig. 10). Differences between CNTL and WV at all three sites are generally small, consistent with the small dewpoint changes observed for this case (Fig. 10). The largest difference occurs at KFWD, where WV moistens the 300–500-hPa layer (Fig. 10b). This is the correct signal for the 375–450-hPa layer but incorrect outside this layer. Overall dewpoint error at this site increases from 5.3 K in CNTL to 6.1 K in WV (Table 4). In the case of 24 May, the only radiosonde side within the domain is located at DDC, but the 0000 UTC sounding for this day was not available (likely not launched due to convection in the area at that time).

For 25 May, operational soundings from Dodge City (DDC) and Topeka (TOP), Kansas, existed at 0000 UTC, along with two MPEX soundings in southern Kansas at 2130 and 2330 UTC (MPX1, MPX2) within the domain. All observations indicate a very dry mid- and upper troposphere, which is generally much drier than the CNTL model analysis at these sites. At MPX1, the boundary layer extends to near 700 hPa, above which the atmosphere dries rapidly (Fig. 11a). Between 700 and 500 hPa, and in a second layer between 400 and 200 hPa, CNTL is far too moist, compared to the observation. The assimilation of $T_{B6.5}$ in the WV experiment dries the 700–500-hPa layer, substantially reducing dewpoint error. This atmospheric layer is significantly below the peak weighting function of the $T_{B6.5}$ channel, which is located at ~375 hPa for a CONUS standard atmosphere (Fig. 1a). However, the mid- and upper-tropospheric moisture conditions for this case are significantly drier than the standard atmosphere, leading to increased sensitivity at lower levels. Sensitivity above this layer remains, as there is a small increase in atmospheric moisture content between 500 and 430 hPa that WV fails to analyze, increasing error at these levels. For MPX1, the average dewpoint error between 700 and 250 hPa decreases from 8.2 K in CNTL to 5.5 K in WV, with WV still being too moist above 400 hPa (Table 4). Similar differences were observed at the MPX2 site (Fig. 11b), with WV being much drier than CNTL in the 600–500-hPa layer, while somewhat missing the moisture between 500 and 450 hPa. For MPX2, dewpoint error decreases from 8.3 to 5.0 K (Table 4). Neither CNTL nor WV seems to resolve this feature. It should be noted that the vertical resolution of the model is rather poor in this region of the atmosphere, with levels located near 520, 480, 440, 410, and 380 hPa. Thus, relatively thin layers of moist or dry air at these levels are likely to be poorly analyzed.

Comparison with the two operational soundings in the domain (DDC and TOP) shows similar results. At DDC, WV is much drier between 600 and 300 hPa and also

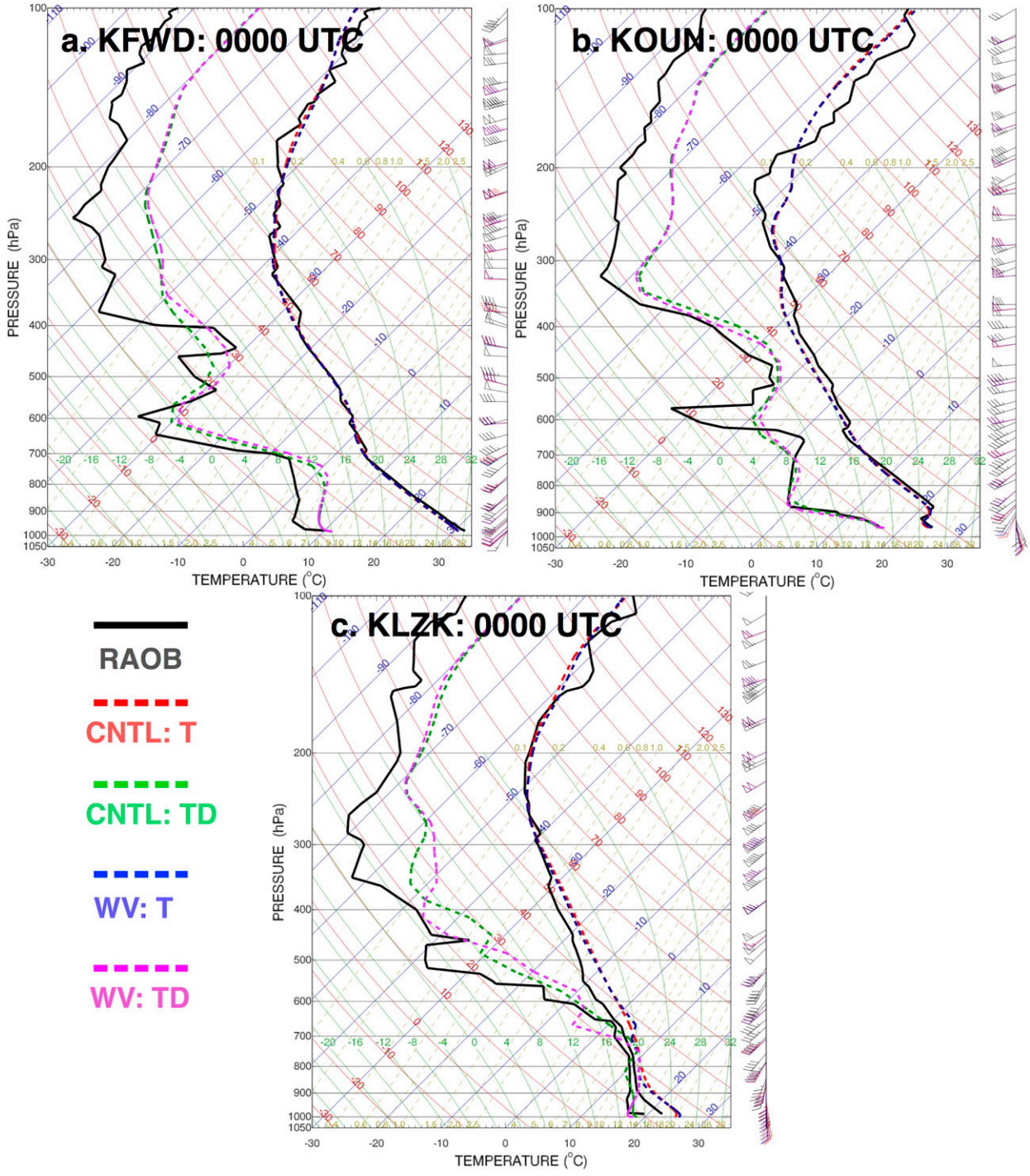


FIG. 9. Observed operational soundings launched at three sites at 0000 UTC 10 May 2016. Black lines indicate observed temperature, dewpoint, and wind profiles. Red and green correspond to CNTL temperature and dewpoint, respectively. Blue and purple correspond to WV temperature and dewpoint, respectively. CNTL and WV winds are denoted as red and blue.

moister at the surface, both consistent with observations (Fig. 11c). Closer inspection of the surface conditions at this site shows that CNTL has a southwest wind, while WV is calm and DDC shows a slight northeasterly wind; thus, WV at DDC has less dry-air advection and greater surface moisture. Whether or not this feature is directly

TABLE 4. Dewpoint error between 700 and 250 hPa between available observed soundings and ensemble mean analyses for both experiments.

| Location | Date | Time (UTC) | CNTL (K) | WV (K) |
|---|---|---|---|---|
| FWD | 10 May | 0000 | 3.8 | 5.1 |
| OUN | 10 May | 0000 | 3.6 | 3.0 |
| LZK | 10 May | 0000 | 6.2 | 6.1 |
| AMA | 23 May | 0000 | 11.3 | 11.3 |
| FWD | 23 May | 0000 | 5.3 | 6.1 |
| OUN | 23 May | 0000 | 6.9 | 6.8 |
| MPX1 | 25 May | 2130 | 8.2 | 5.5 |
| MPX2 | 25 May | 2330 | 8.3 | 5.0 |
| DDC | 26 May | 0000 | 9.6 | 7.1 |
| TOP | 26 May | 0000 | 6.2 | 4.5 |

related to the assimilation of $T_{B6.5}$ is unclear. The eastern-most verification site is TOP, which indicates a boundary layer from the surface to near 750 hPa, which is ~100 hPa deeper than either CNTL or WV. Between 420 and 250 hPa, WV decreases dewpoint, though WV still retains a large dewpoint error (9.6 vs 7.1 K). The verification of CNTL and WV against observations strongly indicates that assimilating $T_{B6.5}$ is correctly drying the mid- and upper troposphere, with the single exception of the thin moist layer observed on the MPEX soundings. The use of sounding data from the Atmospheric Radiation Measurement (ARM) site in northern Oklahoma was considered for several cases, but the quality-controlled soundings were found to be quite noisy, making even a qualitative comparison between observations and model analyses difficult.

In addition to radiosonde verification, it is also possible to assess the impact of assimilating $T_{B6.5}$ by comparing the model analyses against measurements from Aircraft Communication, Addressing, and Reporting System (ACARS) reports from commercial aircraft. However, ACARS measurements bring with them a large set of challenges, including limited spatial and temporal sampling, a lack of vertical profile information except near airports, and relatively low-quality humidity measurements, compared to radiosondes. Despite these limitations, a comparison of CNTL and WV against ACARS dewpoint measurements can yield useful results. Figure 12 shows the location and pressure height of all ACARS dewpoint observations between 1900 and 0000 UTC for each case. Note that most of the observations are centered at major airports, such as DFW on 9 May, AMA and OKC on 22 May, and MCI on 25 May. Since aircrafts are landing and taking off at these locations, the vertical profile of humidity is measured. Otherwise, measurements are generally taken at cruising altitudes above 250 hPa, where limited moisture exists. Dewpoint bias and RMSE between ACARS observations and model analyses at 1900, 2000, 2100, 2200, 2300, and 0000 UTC were calculated and are given in Table 5. The only significant difference between CNTL and WV errors occurs on 9 May, where the bias is lowered by ~0.5 K. This case has the largest ACARS sample size, and the data are placed in a location where WV is clearly making an impact on the environment (Fig. 6). For the other cases, the locations with the maximum impact of assimilating $T_{B6.5}$ are not sampled, resulting in no significant differences in CNTL and WV when comparing against ACARS. Overall, comparisons of CNTL and WV against sounding and ACARS observations clearly indicate that assimilating $T_{B6.5}$ has a measurable impact to the analyzed environment in many regions. However, whether this impact is consistently positive or negative is less clear, especially for the 22 and 24 May cases.

## 6. Reflectivity and updraft helicity forecasts

### *a. Examples*

The most important consideration for this research is how assimilating $T_{B6.5}$ affects the short-term forecasts of high-impact weather events. Since there are seven forecast periods for each of the four cases, an in-depth analysis of each would not be possible in the confines of a single article. Thus, two example forecasts were selected to illustrate both positive and negative impacts from assimilating $T_{B6.5}$. These 2-h forecasts begin at 2200 UTC 9 May and 2330 UTC 25 May. For the 9 May case, 1-km-resolution MRMS composite reflectivity is compared against model-simulated probability matched mean (PMM) composite reflectivity at the analysis time (2200 UTC) and at 30-min forecast intervals thereafter until 0000 UTC (Fig. 13). Probability matching is used to restore amplitudes characteristic of a single member to the ensemble mean (Ebert 2001). A probability matched mean field is created by sorting each value in the ensemble mean and full ensemble from highest to lowest. Values from the full ensemble are then thinned by the number of ensemble members and substituted into the ensemble mean field. A neighborhood with a radius of 15 grid points is used in calculating PMM fields to ensure that ensemble member values occurring near corresponding ensemble mean values are used in the substitution. MRMS reflectivity at 2200 UTC shows a line of severe convection extending from southern Oklahoma into Kansas, with an additional area of precipitation located in northwest Arkansas (Fig. 13a). Both CNTL and WV generate a good representation of the severe convection but significantly overforecast

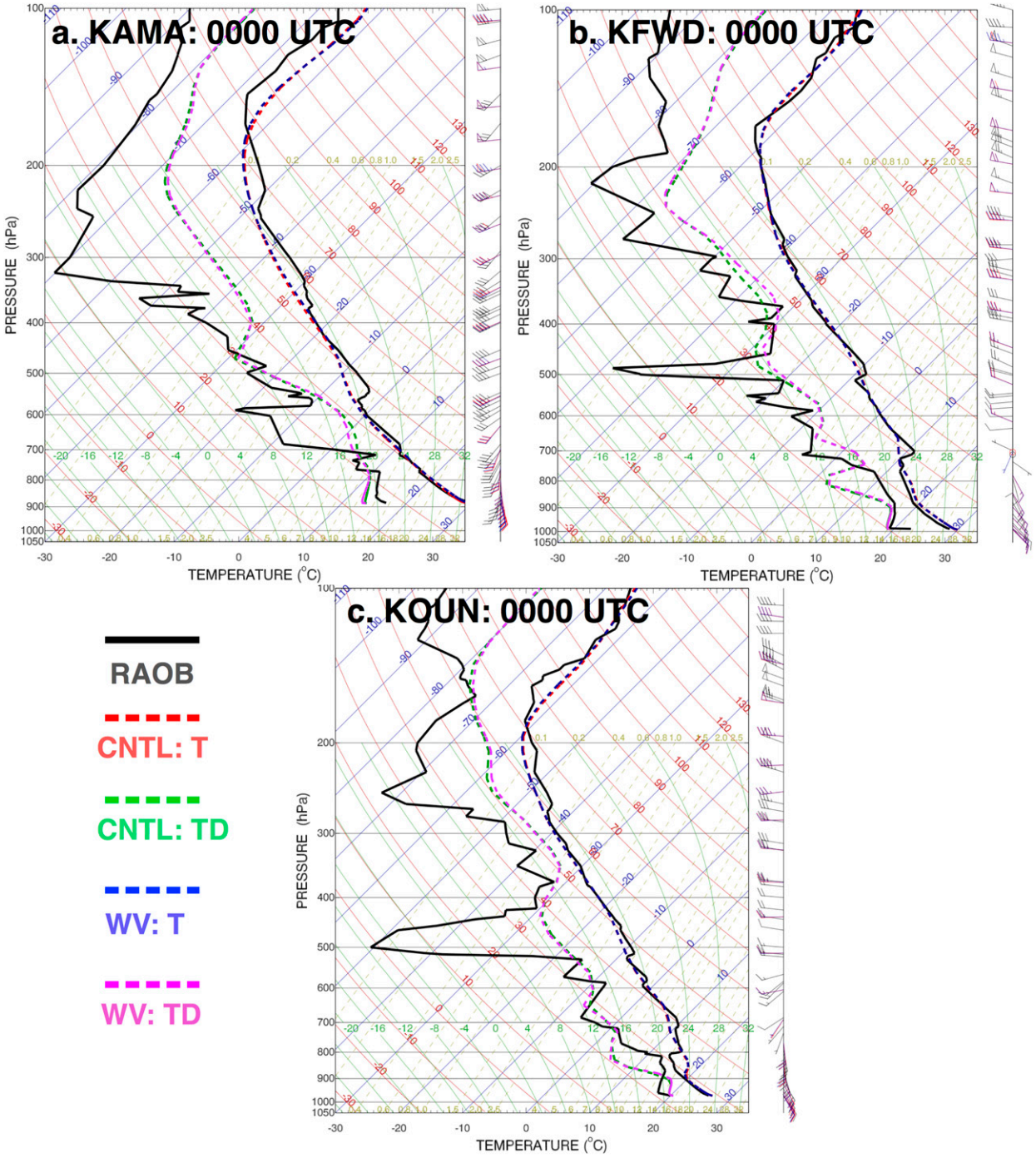


FIG. 10. As in Fig. 9, but for observed operational soundings launched at three sites at 0000 UTC 23 May 2016.

precipitation in AR (Figs. 13b,c). CNTL and WV differ in this aspect, with the latter generating much less precipitation, thereby better matching observations. Similar characteristics are apparent at 2230 UTC (Figs. 13d–f). By 2300 UTC, the coverage of precipitation in Arkansas has increased in the WV experiment and is now similar to CNTL (Figs. 13g–i). The representation of convection in southern Oklahoma is similar. After 2300 UTC, WV differs from CNTL in this area by maintaining the southern Oklahoma storms as two clearly defined supercells, while CNTL weakens the northern supercell more

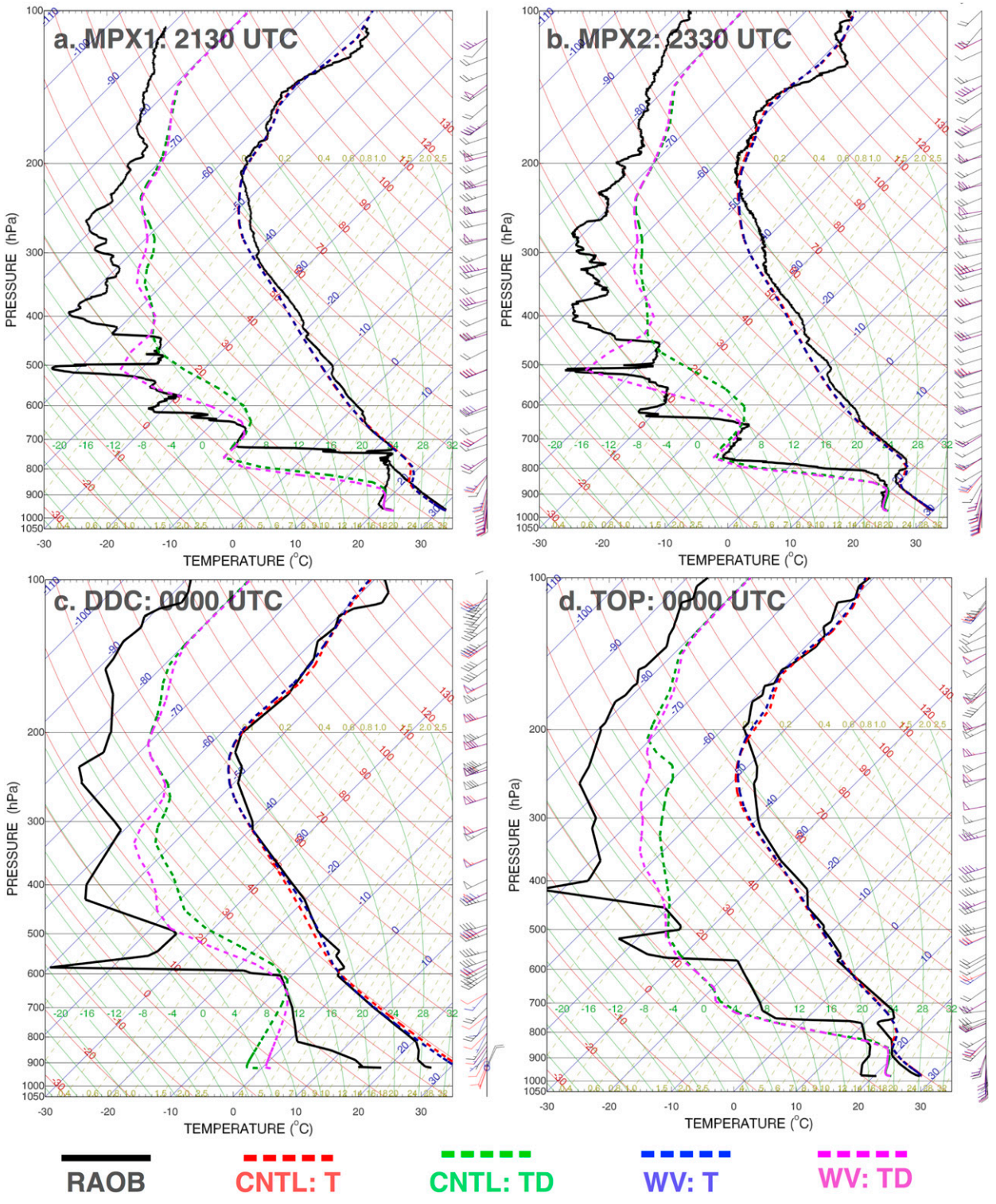


FIG. 11. As in Fig. 9, but for observed MPEX and operational soundings launched at four sites in Kansas on 25–26 May 2016.

rapidly (Figs. 13j–o). Corresponding MRMS data show individual convective cores >55 dB$Z$ remain at 0000 UTC (Fig. 13m).

Larger differences between CNTL and WV can be seen when analyzing forecasts in a probabilistic framework. Figure 14 shows the probability of composite

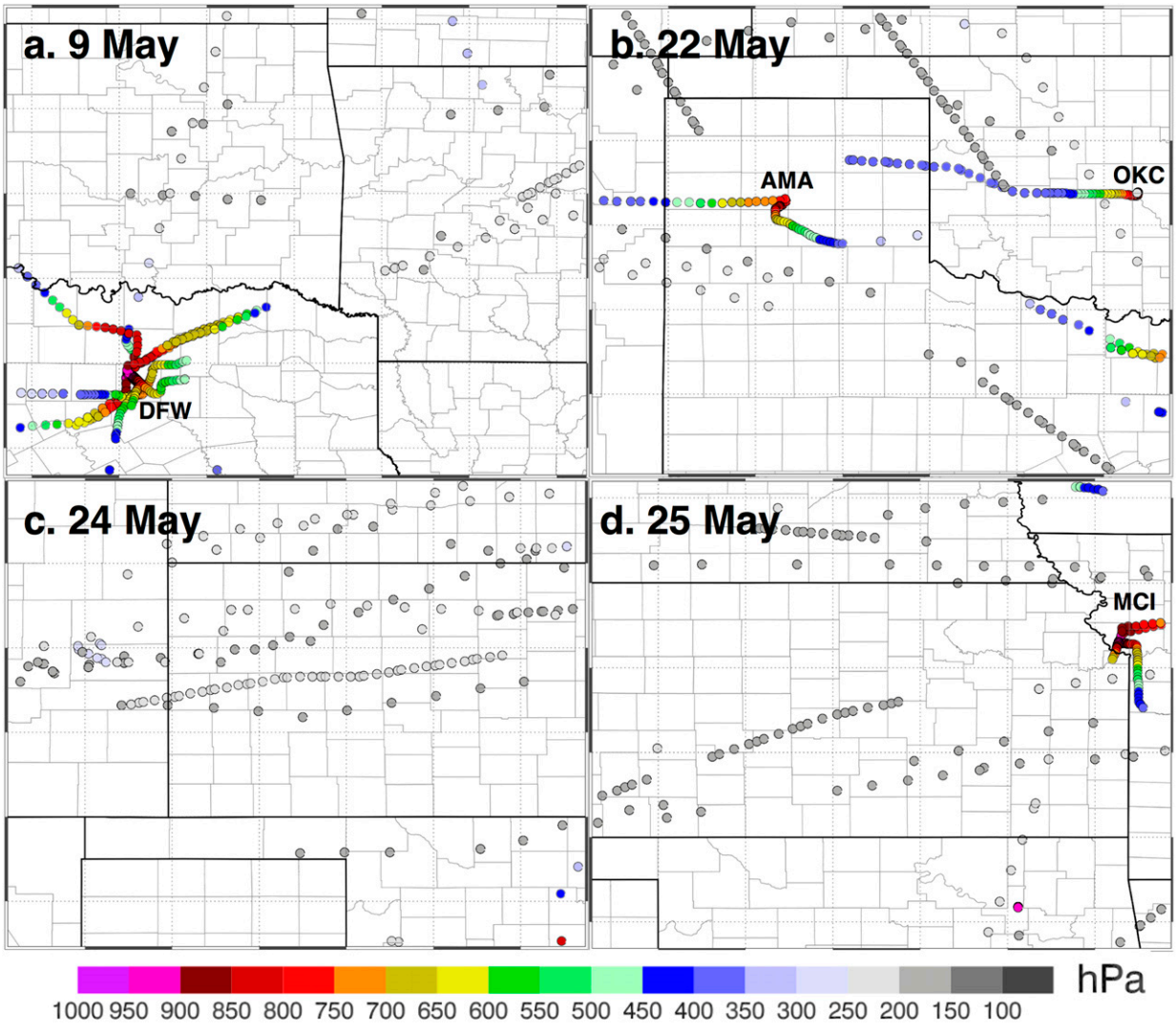


FIG. 12. Locations of ACARS dewpoint observations for each case between 1900 and 0000 UTC, with colors indicating pressure height of each observation. Major airports associated with observations within each domain are labeled.

reflectivity >40 dB$Z$ and 2–5-km updraft helicity >60 $m^2 s^{-2}$ over the 2-h forecast period for both experiments with severe weather reports during that time period overlaid. CNTL generates moderate (>50%) probability reflectivity swaths associated with the southern Oklahoma convection that persist for the entire forecast period (Fig. 14a). The ''right turn'' for these supercells is also evident. Shorter swaths are present in north-central Oklahoma, indicating weakening convection, with a large area of high probabilities in southern Kansas associated with nonsupercell convection. Additional moderate probability swaths with a southwest to northeast orientation are located in Arkansas. Corresponding updraft helicity (UH) tracks generally have much lower probabilities (Fig. 14b). The only tracks of significance are associated with the southern Oklahoma supercells, with one maintaining 30%–40% probabilities and the other >50% probabilities. Both generated several tornadoes during this

TABLE 5. Dewpoint bias and RMSE between ACARS observations and ensemble mean analyses for each case aggregated over analysis times 1900, 2000, 2100, 2200, 2300, and 0000 UTC.

| | | Bias | | RMSE | |
|---|---|---|---|---|---|
| Event | Number | CNTL | WV | CNTL | WV |
| 9 May | 365 | −1.23 | −0.76 | 4.54 | 4.48 |
| 22 May | 234 | −1.14 | −1.15 | 4.08 | 4.12 |
| 24 May | 157 | 0.05 | −0.04 | 4.02 | 4.00 |
| 25 May | 178 | −1.98 | −2.01 | 4.12 | 4.16 |

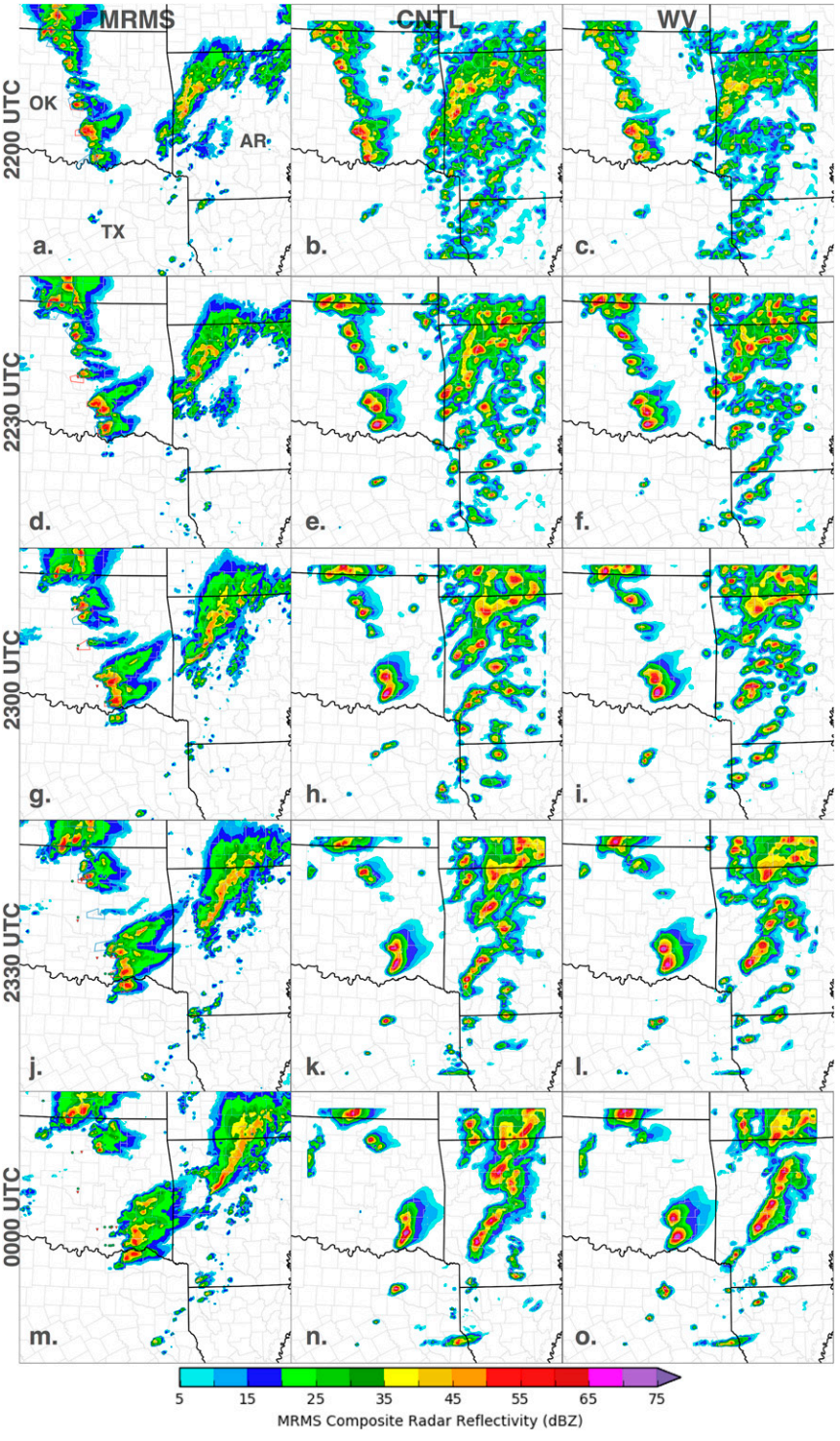


FIG. 13. Observed MRMS composite reflectivity and corresponding CNTL and WV PMM composite reflectivity analyses and forecasts at 2200 UTC and 30-min intervals afterward until 0000 UTC.

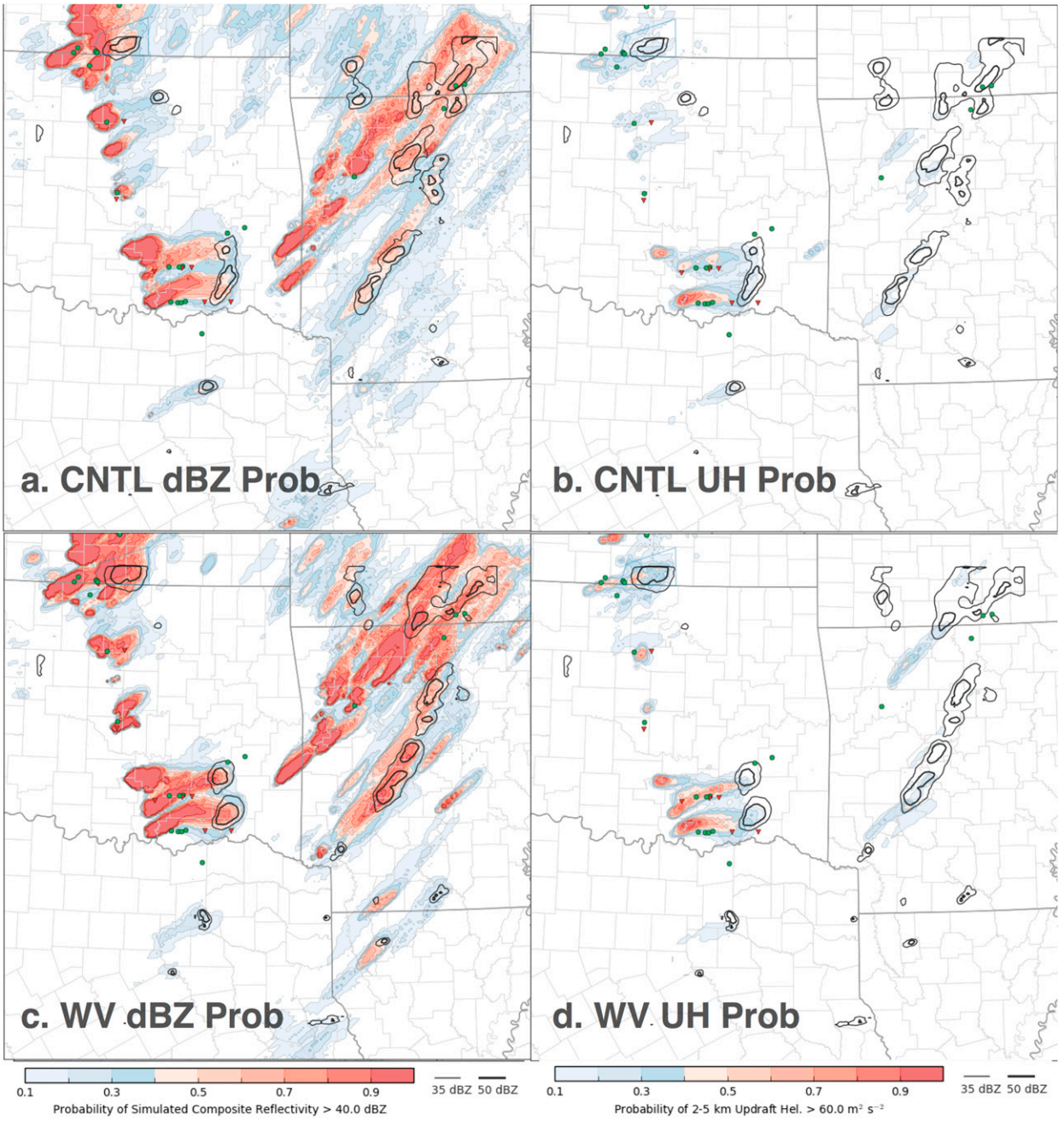


FIG. 14. Probability of simulated composite reflectivity from each ensemble member >40 dB$Z$ and 2–5-km UH > 60 $m^2 s^{-2}$ for the 2-h forecast period beginning at 2200 UTC 9 May for both CNTL and WV experiments. Black contours indicate PMM reflectivity at 25 and 40 dB$Z$ at the end of the 2-h forecast period. Green dots represent severe hail reports, blue squares represent severe wind reports, and red inverted triangles represent tornado reports during the 2-h forecast period.

forecast period. Elsewhere, probabilities are generally less than 20%, even for tornadic storms in north-central Oklahoma.

Reflectivity and UH probabilistic forecasts generated from WV differ from CNTL in several important aspects. Reflectivity probabilities associated with the southern Oklahoma supercells generally exceed 80%, indicating that more ensemble members maintain these storms in the forecast (Fig. 14c). Farther north, higher probabilities are also apparent with the north-central

Oklahoma storm that generated a single tornado report at 2221 UTC. In Arkansas, the forecast is similar to CNTL, but with less spread and more defined storm tracks. The UH forecasts generated by WV also differ, producing higher UH probabilities for the southern Oklahoma supercells, compared to CNTL (Fig. 14d). The largest difference is for the more northern of these two supercells, with probabilities increasing from <40% to near 70%. Also, WV generates small areas of >50% UH probabilities associated with the other tornadic storms in Oklahoma, compared to almost no probability from CNTL, and has a lower false alarm signal for the north Texas storm. These results indicate that for this forecast period, assimilating $T_{B6.5}$ modifies the model environment in such a way as to make it favorable for rotating supercells to persist in Oklahoma, while decreasing favorability in Arkansas. The key difference is an increase in ensemble mean convective available potential energy (CAPE) and a corresponding decrease in convective inhibition (CIN) in southeast Oklahoma (Fig. 15).

While assimilating $T_{B6.5}$ generated a positive impact for the example above, the results for a forecast originating at 2330 UTC 25 May were much different. At 2330 UTC, MRMS reflectivity shows an isolated supercell located in north-central Kansas, with attempts at storm development farther south (Fig. 16a). This case differs from the other three cases in several important ways. On 25 May, midtropospheric conditions were much drier than for the other events. Recall that the model has a consistent moist bias relative to available observations (Fig. 11). Also, overall dynamic forcing was limited, significantly reducing convective initiation relative to the other cases. Finally, much of the domain was completely cloud free, allowing for warmer temperatures, but also increased mixing that reduced the amount of moisture as the afternoon progressed. As a result of these factors, only a single supercell developed in Kansas, compared to the much more widespread convection observed in the other cases. Both CNTL and WV correctly analyze the primary storm, with the differences between the two experiments being small (Figs. 16b,c). As forecast time increases, the size and magnitude of forecast PMM reflectivity by WV decreases relative to CNTL, indicating that WV is weakening the storm too quickly. MRMS observations show that the supercell maintains itself throughout this 2-h period with additional development occurring in northern Oklahoma, which is not forecast by either CNTL or WV. By 0130 UTC, both experiments appear to be incorrectly weakening the storm, but WV is clearly weakening it faster (Figs. 16m–o). Probabilistic forecasts of reflectivity and UH are consistent with the PMM reflectivity forecasts. CNTL generates both higher reflectivity and UH probability swaths associated with this storm than does WV (Fig. 17). In particular, the UH probabilities are much lower, indicating that many members fail to retain supercell characteristics with increasing forecast time. Evidence suggests that the saturated updraft parcels are mixing with the drier atmosphere in WV, causing analyzed convection to prematurely weaken in the model forecast. The drier atmosphere in WV also increases CIN slightly, compared to CNTL, ahead of the supercell at 2330 UTC (not shown). Finally, Gilmore and Wicker (1998) noted that very dry midlevel air resulted in low-level outflow that outran the corresponding midlevel mesocyclone, subsequently leading to weakening of the overall storm. Comparison of the storm morphology between CNTL and WV is consistent with these observations.

Recall that assimilating $T_{B6.5}$ often dried the mid- and upper troposphere in the model analysis, better matching the very dry conditions observed in the various soundings. Also, the observations indicated that both experiments failed to capture the depth of the boundary layer moisture present for this day, even though both generate high ($>4000\,J\,kg^{-1}$) and low CIN ($<25\,J\,kg^{-1}$) environments. Given the very dry nature of the mid- and upper troposphere, any underestimation of boundary layer moisture will have a negative impact on the analyzed environment's ability to support convection. Thus, assimilating $T_{B6.5}$ correctly reduces a moist bias in the mid- and upper troposphere, but at the same time reduces the favorability of the environment to support convection, given the already underestimated boundary layer moisture.

### b. *Object-based verification*

The overall accuracy of ensemble forecasts for each event is assessed using object-based verification (e.g., Davis et al. 2006a,b). Simulated composite reflectivity and 30-min, 2–5-km UH fields for each available forecast time step are compared to corresponding verification fields derived from MRMS composite reflectivity and range-corrected azimuthal wind shear (Newman et al. 2013). Objects are initially defined as coherent regions exceeding thresholds of 40 dB$Z$ or the 99.95th gridpoint percentile value in the composite reflectivity or updraft helicity/azimuthal wind shear fields (hereafter labeled as rotation objects). Reflectivity objects are then subjected to an area threshold of 10 grid points and rotation track objects to both area and continuity thresholds of 10 grid points and greater than two time steps, respectively, to limit the number of spurious objects in the dataset. Forecast and verification objects are

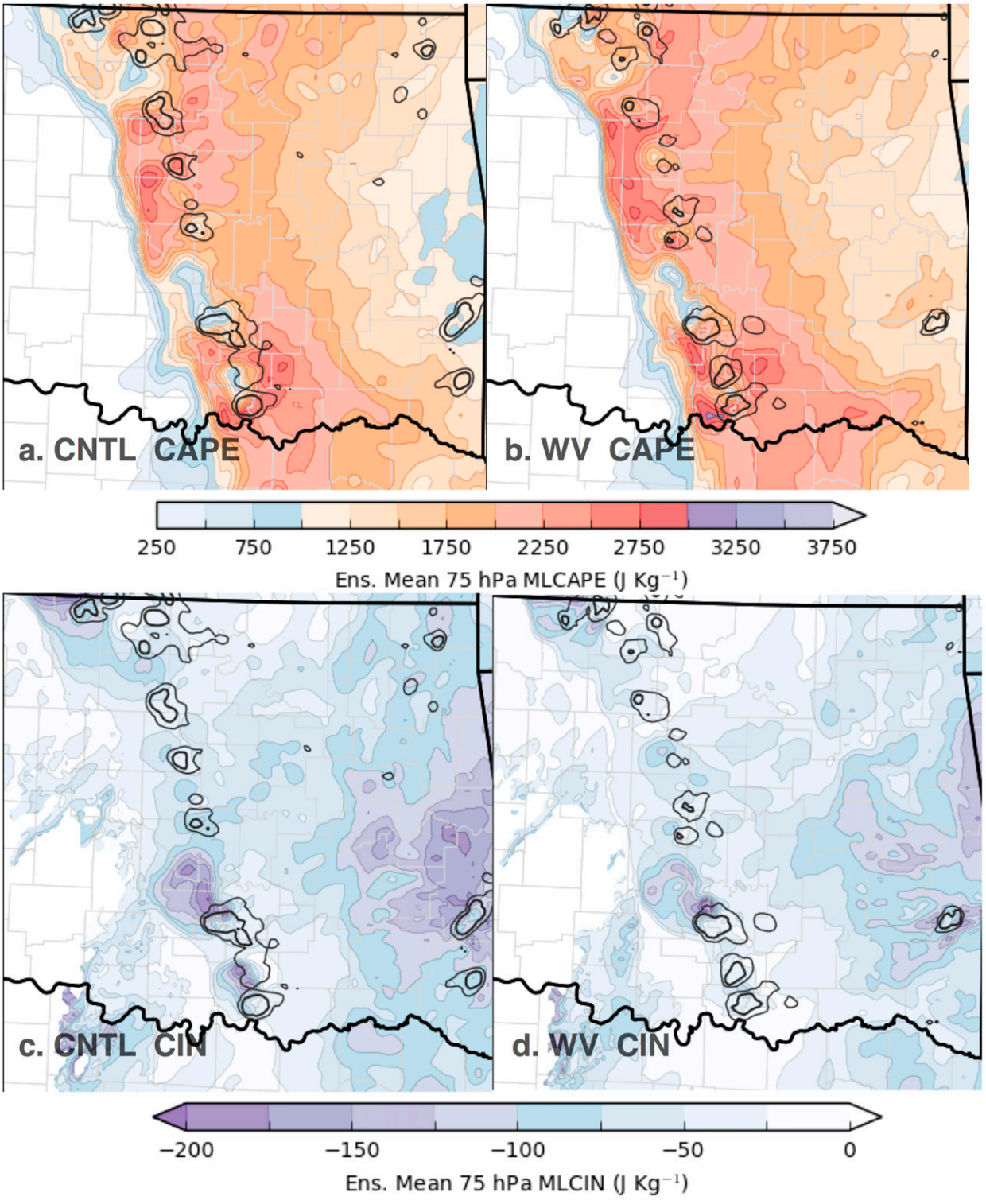


FIG. 15. Ensemble mean 75-hPa mean–layer CAPE and CIN for the CNTL and WV experiments at 2200 UTC 9 May.

matched using a simple total interest score similar to Skinner et al. (2016) and based on the Method for Object-based Diagnostic Evaluation (MODE; Davis et al. 2006a,b). Components of the total interest score are limited to displacement in space and time with maximum allowable centroid distance (time)

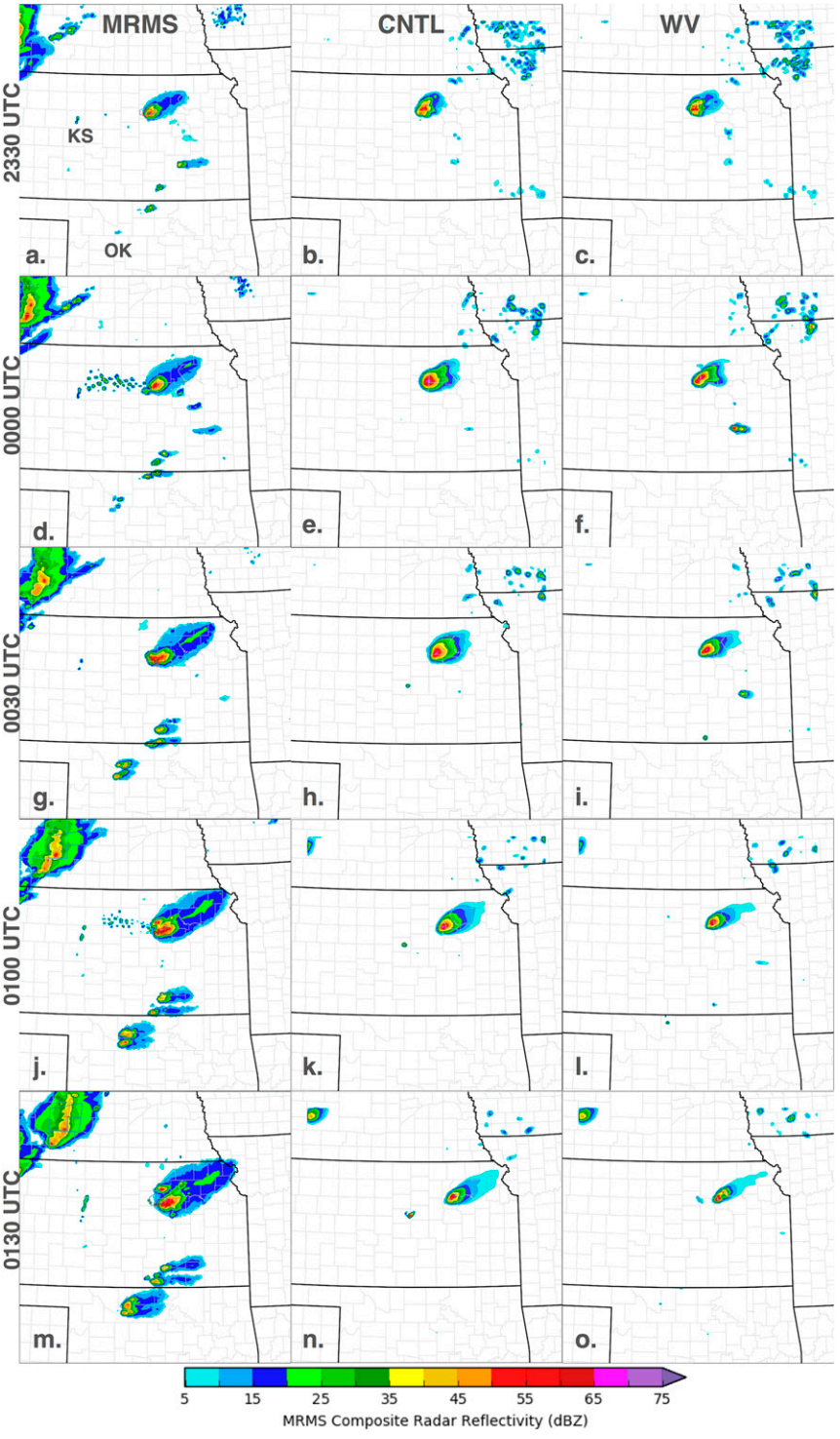


FIG. 16. Observed MRMS composite reflectivity and corresponding CNTL and WV PMM composite reflectivity analyses and forecasts at 2330 UTC and 30-min intervals afterward until 0130 UTC.

displacements of 40 km (20 min). Object pairs with a total interest score exceeding 0.2 are matched and considered ''hits,'' with forecast objects that are not matched to an observed object considered ''false alarms.'' The maximum space and time displacement radii and total interest thresholds used in object

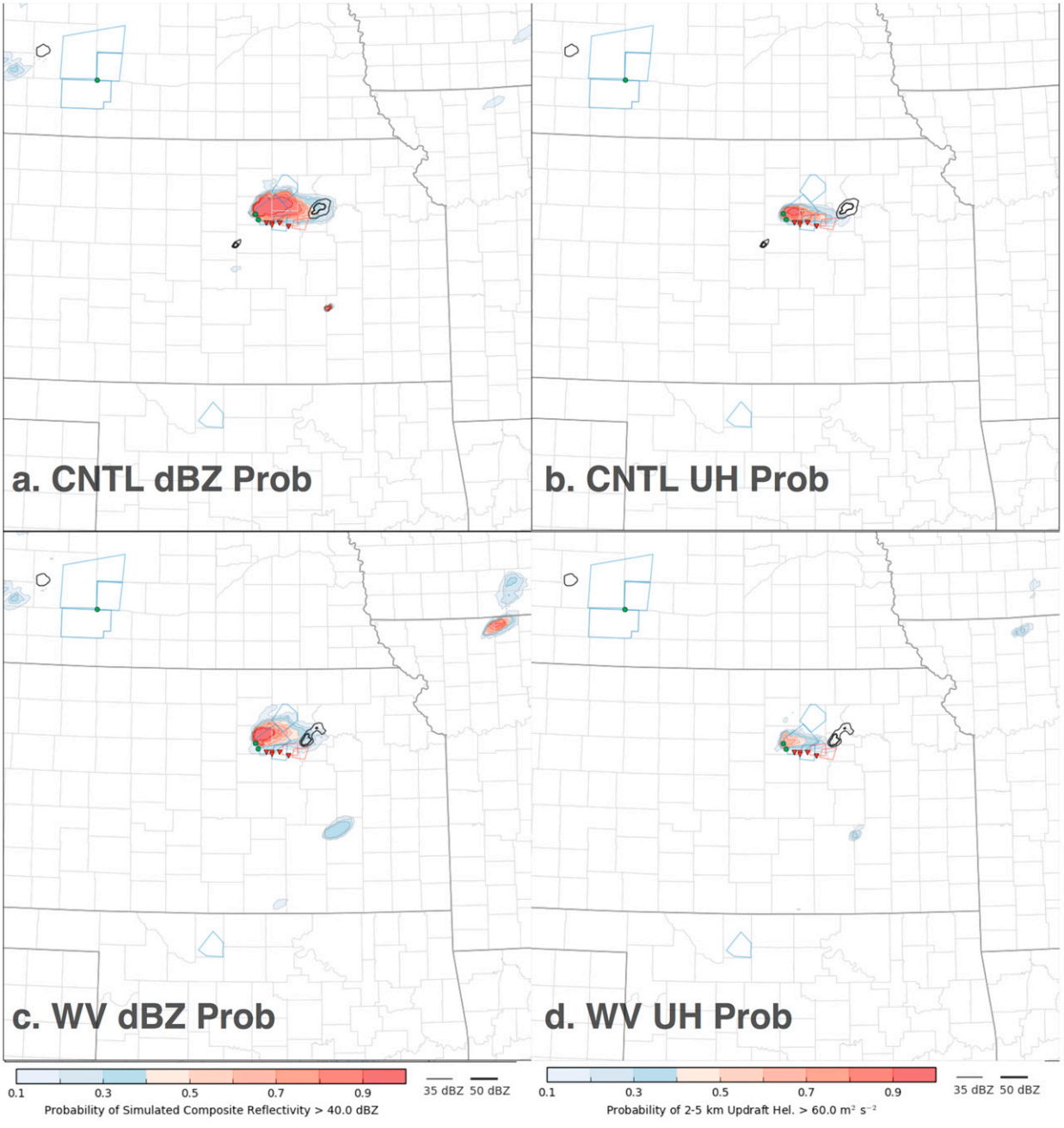


FIG. 17. Probability of simulated composite reflectivity from each ensemble member >40 dB$Z$ and 2–5-km UH > 60 $m^2 s^{-2}$ for the 2-h forecast period beginning at 2330 UTC 25 May for both CNTL and WV experiments.

matching have been chosen through trial and error (Skinner et al. 2016). The highly configurable nature of object definition and matching is a limitation of object-based methods (e.g., Wolff et al. 2014). However, it is noted that while verification scores are sensitive to object-matching thresholds, qualitative comparisons between different datasets remain similar (Skinner et al. 2016, their Fig. A1). Object matching is performed on each ensemble member for each forecast initialization time for a particular case. Classification of objects as hits and false alarms allows contingency-table-based verification metrics (Wilks 2006) to be calculated for each ensemble member. The verification metrics, specifically critical success index (CSI), from each member and forecast time for a particular case are averaged to show the ensemble mean skill for all forecast periods.

TABLE 6. Number of reflectivity and rotation objects accumulated over all members and forecast times for each case for both CNTL and WV experiments.

| | dBZ | | Rotation | |
|---|---|---|---|---|
| Event | CNTL | WV | CNTL | WV |
| 19 May | 80 573 | 71 828 | 11 666 | 13 773 |
| 22 May | 23 871 | 23 591 | 13 292 | 13 460 |
| 24 May | 28 200 | 28 633 | 16 652 | 16 199 |
| 25 May | 2836 | 3037 | 1223 | 958 |
| Total | 135 480 | 127 089 | 42 833 | 44 390 |

The number of reflectivity and rotation objects for each case is provided in Table 6. The greatest number of objects occurs on 9 May, with over 71 000 reflectivity and 11 000 rotation objects generated by both experiments. The WV experiment generates several thousand fewer reflectivity objects, compared to CNTL, which is consistent with the decrease in precipitation present in Arkansas in the early forecast period (Fig. 13). However, WV generates over 2000 more rotation objects, indicating that forecast convection is more likely to maintain supercell characteristics than in CNTL. For 9 May, WV generates a higher CSI for reflectivity than CNTL for the first ~30 min of the forecast period, after which both become similar (Fig. 18a). This difference is primarily attributable to a decrease in false alarm objects occurring in Arkansas. Overall probability of detection is similar. The difference between CNTL and WV is larger when comparing CSI for rotation objects, with WV generating higher CSI scores out to at least 60 min (Fig. 18b). This is consistent with the higher UH probabilities forecast by WV in the 9 May example shown in Fig. 14d.

For 22 and 24 May, the object counts are similar for both experiments. Both 22 and 24 May events indicate little improvement in CSI for reflectivity from assimilating $T_{B6.5}$; however, some improvement in rotation object CSI is evident (Figs. 18c–f). While the differences are not large, WV consistently generates higher overall CSI for rotation objects, compared to CNTL for 60+ min forecasts. The 25 May case generates far fewer objects since only a single supercell is present within the model domain, compared to more widespread coverage in the other cases. This case generates substantially different results, with WV reflectivity and rotation forecasts performing much worse for forecast periods out to 1 h (Figs. 18g,h). These results are consistent with the example where WV failed to maintain the supercell in many members. Note that CSI for several WV members actually falls to zero after 40 min have elapsed. In addition, WV also generates a small area of ''spurious'' convection in southern Kansas in later forecast periods that is associated with developing convection in northern Oklahoma, but not close enough to it to cause a hit (not shown). The combination of a poor forecast of the primary storm, a near miss, and the small object sample size generates the poor CSI for this case.

Contingency table statistics are also calculated for the entire set of 28 forecast cycles over all four cases to assess the overall impact of assimilating $T_{B6.5}$ for these events. The total number of reflectivity and rotation objects is approximately 130 000 and 43 000, respectively (Table 6). The 9 May event accounts for over 50% of the reflectivity objects, while the 9, 22, and 24 May events each account for roughly one-third of the rotation objects. The small number of objects generated by the 25 May case limits its impact to the bulk statistics. Figure 19 provides overall CSI for reflectivity (Fig. 19a) and rotation (Fig. 19b) objects, showing that the WV experiments have some skill over the non-WV experiments for the first 30 min of the forecast period for reflectivity and for at least 1 h in the case of 2–5-km UH. Corresponding probability of detection (POD) and false alarm rate (FAR) for the combined sample shows that the primary contributor to improving forecast skill for reflectivity is a reduction in false alarms (Figs. 19c–f). Conversely, the WV experiments decrease FAR and increase POD associated with UH throughout much of the forecast period, indicating a greater impact on the forecast of rotating storms versus overall precipitation.

## 7. Conclusions

Assimilating $T_{B6.5}$ during four high-impact weather events occurring in May 2016 modified the mid- and upper-level moisture analysis and resulting forecasts of reflectivity and rotation. In general, assimilating $T_{B6.5}$ had the expected impact on the analysis, with positive $T_{B6.5}$ innovations resulting in drying and negative innovations resulting in an increase in moisture. A completed verification of the environmental differences was not possible due to limited midtropospheric observations, but available radiosonde and ACARS measurements did indicate improvement in at least two cases. For 9 May, radiosonde and ACARS measurements indicate a decrease in the midtropospheric moisture bias in north Texas. For 25 May, large improvements in the moisture analysis were observed at all four of the radiosonde sites available. The impact on reflectivity and rotation forecasts was mixed with reflectivity forecasts only being improved for the 9 May case, but rotation object forecasts being improved for three cases (9, 24, and 25 May) out to at least 60 min. However, a large reduction in both reflectivity and rotation skill was observed for the 25 May case. Still, the improvement

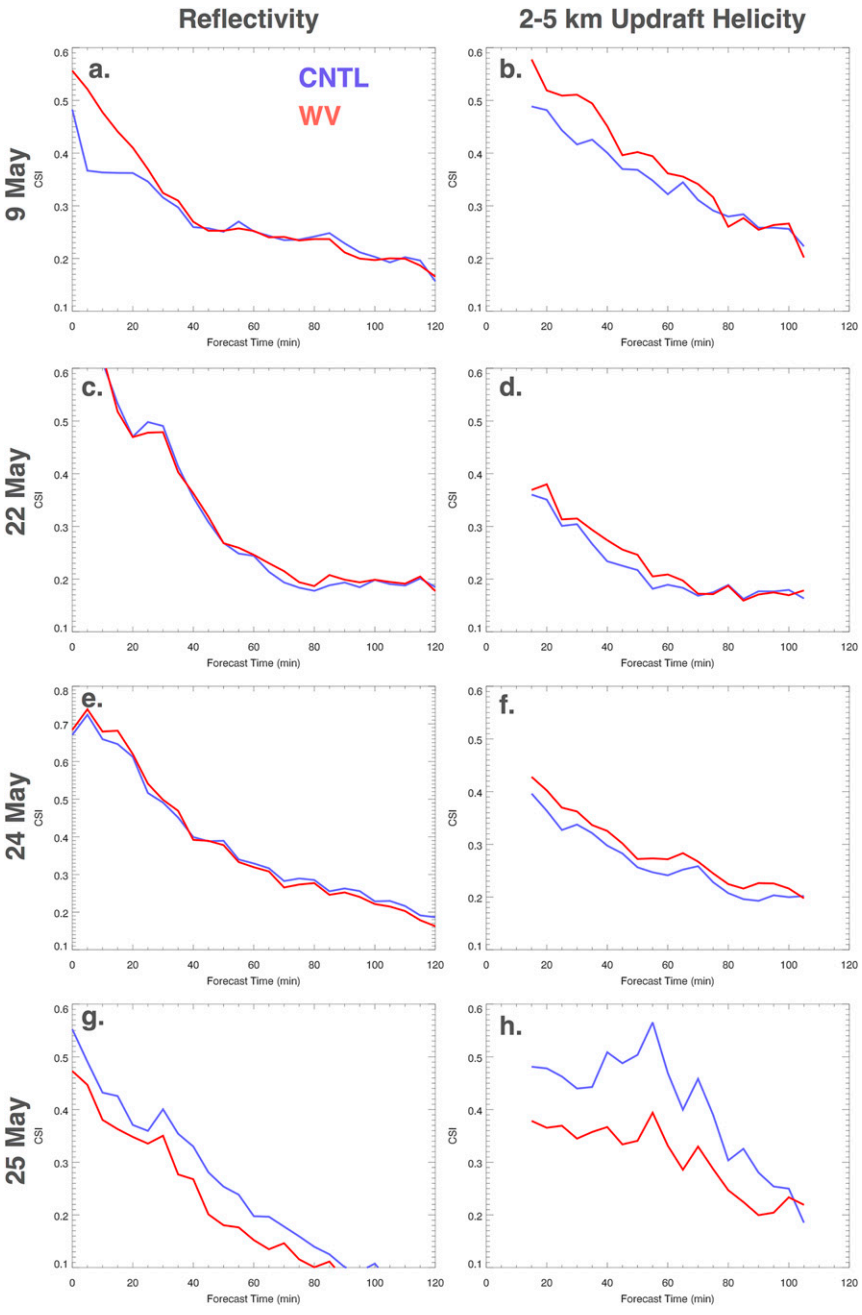


FIG. 18. CSI for reflectivity and UH averaged over seven 2-h forecast periods for each case and experiment.

observed in the first three cases indicates there is potential to study the impact of assimilating water vapor sensitive radiances further.

Many challenges remain to fully take advantage of radiance assimilation in a WoF system, as demonstrated by the results from the 25 May event. In this case, radiance assimilation has the correct impact on the analyzed mid- and upper-tropospheric environment, but the "improved" environment resulted in less skillful supercell forecasts. Model uncertainties and biases in the model analysis within the boundary layer are not significantly impacted by the assimilation of $T_{B6.5}$; thus, negative aspects of these conditions could not be corrected. Improving this portion of the analysis will require a network of surface-based profilers that can measure boundary layer temperature and

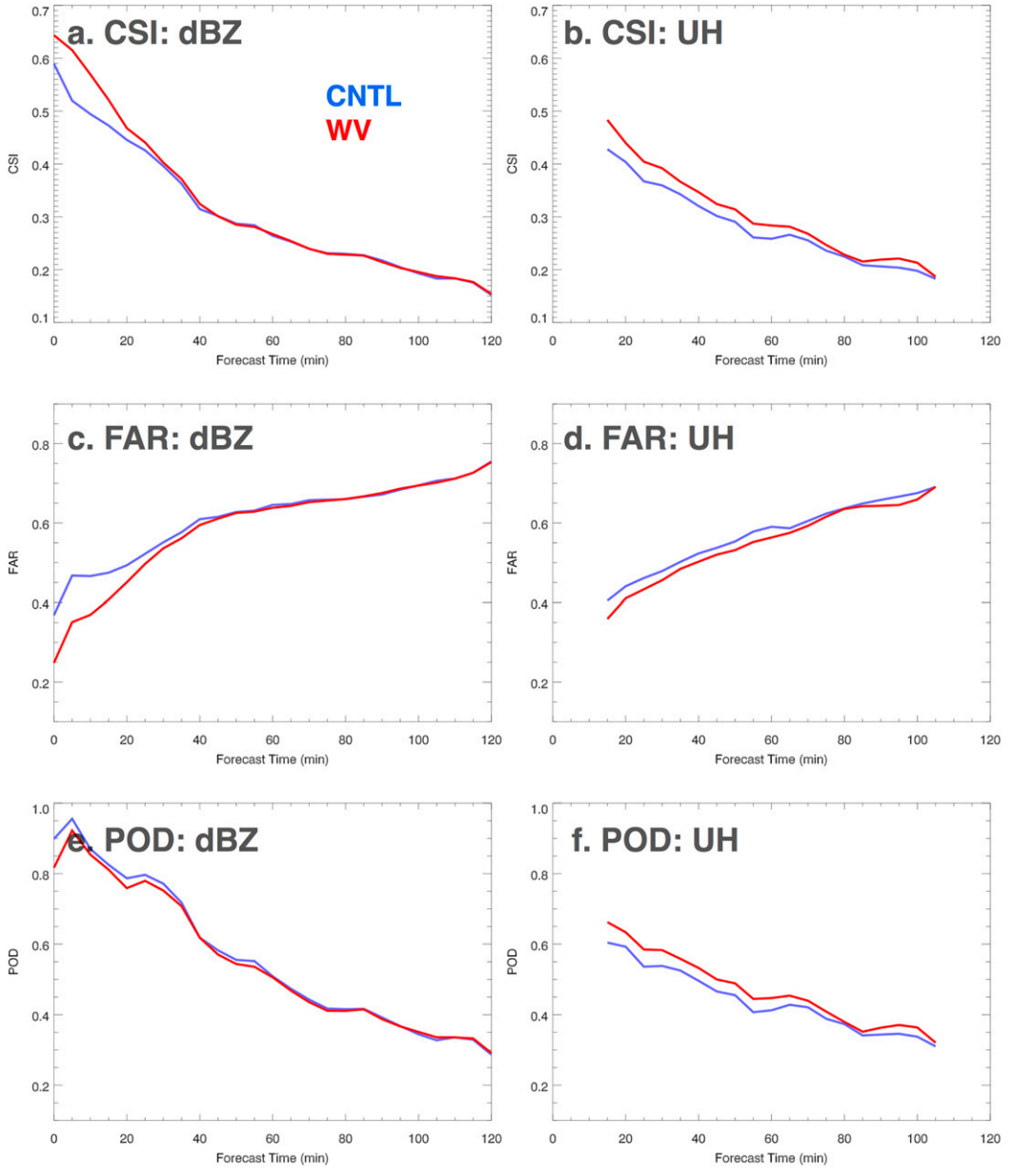


FIG. 19. CSI, FAR, and POD for reflectivity and 2–5-km UH averaged over seven 2-h forecast periods aggregated over all cases.

moisture conditions that cannot be adequately resolved from satellite data. This also indicates that additional research into correction of inherent model biases is required in the future. Still, GOES imager data show promise in adjusting the mid- and upper-tropospheric conditions closer to observations and the additional channels provided by the ABI on board the recently launched *GOES-16* satellite have the potential have a greater positive impact on the model environment.

*Acknowledgments.* Funding for this research was provided by NASA ROSES NNX15AR57G with additional support provided by the NOAA/Office of Oceanic and Atmospheric Research under NOAA–University of Oklahoma Cooperative Agreement NA11OAR4320072 and NA16OAR4320115, under the U.S. Department of Commerce. MPEX soundings used for environmental verification were provided by Dr. Michael Conigilio. CWP observations were derived from the SAT-CORPS product generated by NASA Langley Research Center.

GOES imager weighting function data used in Fig. 1 were provided by Mat Gunshor from CIMSS at the University of Wisconsin. The second, fourth, and fifth authors are also supported by NA11OAR4320072 and AGS-1359703.

## REFERENCES


Aksoy, A., D. Dowell, and C. Snyder, 2009: A multicase comparative assessment of the ensemble Kalman filter for assimilation of radar observations. Part I: Storm-scale analyses. *Mon. Wea. Rev.*, **137**, 1805–1824, https://doi.org/10.1175/2008MWR2691.1.

——, ——, and ——, 2010: A multicase comparative assessment of the ensemble Kalman filter for assimilation of radar observations. Part II: Short-range ensemble forecasts. *Mon. Wea. Rev.*, **138**, 1273–1292, https://doi.org/10.1175/2009MWR3086.1.

Anderson, J. L., and N. Collins, 2007: Scalable implementations of ensemble filter algorithms for data assimilation. *J. Atmos. Oceanic Technol.*, **24**, 1452–1463, https://doi.org/10.1175/JTECH2049.1.

——, T. Hoar, K. Raeder, H. Liu, N. Collins, R. Torn, and A. Avellano, 2009: The Data Assimilation Research Testbed: A community facility. *Bull. Amer. Meteor. Soc.*, **90**, 1283–1296, https://doi.org/10.1175/2009BAMS2618.1.

Auligné, T., and A. P. McNally, 2007: Interaction between bias correction and quality control. *Quart. J. Roy. Meteor. Soc.*, **133**, 643–653, https://doi.org/10.1002/qj.57.

——, ——, and D. P. Dee, 2007: Adaptive bias correction for satellite data in a numerical weather prediction system. *Quart. J. Roy. Meteor. Soc.*, **133**, 631–642, https://doi.org/10.1002/qj.56.

Benjamin, S. G., and Coauthors, 2016: A North American hourly assimilation and model forecast cycle: The Rapid Refresh. *Mon. Wea. Rev.*, **144**, 1669–1694, https://doi.org/10.1175/MWR-D-15-0242.1.

Davis, C. A., B. G. Brown, and R. G. Bullock, 2006a: Object-based verification of precipitation forecasts. Part I: Methodology and application to mesoscale rain areas. *Mon. Wea. Rev.*, **134**, 1772–1784, https://doi.org/10.1175/MWR3145.1.

——, ——, and ——, 2006b: Object-based verification of precipitation forecasts. Part II: Application to convective rain systems. *Mon. Wea. Rev.*, **134**, 1785–1795, https://doi.org/10.1175/MWR3146.1.

Dee, D. P., and S. Uppala, 2009: Variational bias correction of satellite radiance data in the ERA-Interim reanalysis. *Quart. J. Roy. Meteor. Soc.*, **135**, 1830–1841, https://doi.org/10.1002/qj.493.

Derber, J. C., and W.-S. Wu, 1998: The use of TOVS cloud-cleared radiances in the NCEP SSI analysis system. *Mon. Wea. Rev.*, **126**, 2287–2299, https://doi.org/10.1175/1520-0493(1998)126<2287:TUOTCC>2.0.CO;2.

Dowell, D., and L. J. Wicker, 2009: Additive noise for storm-scale ensemble data assimilation. *J. Atmos. Oceanic Technol.*, **26**, 911–927, https://doi.org/10.1175/2008JTECHA1156.1.

——, F. Zhang, L. J. Wicker, C. Snyder, and N. A. Crook, 2004: Wind and temperature retrievals in the 17 May 1981 Arcadia, Oklahoma, supercell: Ensemble Kalman filter experiments. *Mon. Wea. Rev.*, **132**, 1982–2005, https://doi.org/10.1175/1520-0493(2004)132<1982:WATRIT>2.0.CO;2.

——, L. J. Wicker, and C. Snyder, 2011: Ensemble Kalman filter assimilation of radar observations of the 8 May 2003 Oklahoma City supercell: Influences of reflectivity observations on storm-scale analyses. *Mon. Wea. Rev.*, **139**, 272–294, https://doi.org/10.1175/2010MWR3438.1.

Dudhia, J., 1989: Numerical study of convection observed during the Winter Monsoon Experiment using a mesoscale two-dimensional model. *J. Atmos. Sci.*, **46**, 3077–3107, https://doi.org/10.1175/1520-0469(1989)046<3077:NSOCOD>2.0.CO;2.

Ebert, E., 2001: Ability of a poor man's ensemble to predict the probability and distribution of precipitation. *Mon. Wea. Rev.*, **129**, 2461–2480, https://doi.org/10.1175/1520-0493(2001)129<2461:AOAPMS>2.0.CO;2.

Fabry, F., and J. Sun, 2010: For how long should what data be assimilated for the mesoscale forecasting of convection and why? Part I: On the propagation of initial condition errors and their implications for data assimilation. *Mon. Wea. Rev.*, **138**, 242–255, https://doi.org/10.1175/2009MWR2883.1.

Gallo, B. T., and Coauthors, 2017: Breaking new ground in severe weather prediction: The 2015 NOAA/Hazardous Weather Testbed spring forecasting experiment. *Wea. Forecasting*, **32**, 1541–1568, https://doi.org/10.1175/WAF-D-16-0178.1.

Gaspari, G., and S. E. Cohn, 1999: Construction of correlation functions in two and three dimensions. *Quart. J. Roy. Meteor. Soc.*, **125**, 723–757, https://doi.org/10.1002/qj.49712555417.

Gilmore, M. S., and L. J. Wicker, 1998: The influence of midtropospheric dryness on supercell morphology and evolution. *Mon. Wea. Rev.*, **126**, 943–958, https://doi.org/10.1175/1520-0493(1998)126<0943:TIOMDO>2.0.CO;2.

Han, Y., F. Weng, Q. Liu, and P. van Delst, 2007: A fast radiative transfer model for SSMIS upper atmosphere sounding channels. *J. Geophys. Res.*, **112**, D11121, https://doi.org/10.1029/2006JD008208.

Harris, B. A., and G. Kelly, 2001: A satellite radiance-bias correction scheme for data assimilation. *Quart. J. Roy. Meteor. Soc.*, **127**, 1453–1468, https://doi.org/10.1002/qj.49712757418.

Hong, S.-Y., Y. Noh, and J. Dudhia, 2006: A new vertical diffusion package with an explicit treatment of entrainment processes. *Mon. Wea. Rev.*, **134**, 2318–2341, https://doi.org/10.1175/MWR3199.1.

Hu, M., H. Shao, D. Stark, K. Newman, C. Zhou, and X. Zhang, 2016: Gridpoint Statistical Interpolation (GSI) user's guide version 3.5. Developmental Testbed Center Rep., 141 pp., https://dtcenter.org/com-GSI/users/docs/users_guide/GSIUserGuide_v3.5.pdf.

Iacono, M. J., J. S. Delamere, E. J. Mlawer, M. W. Shephard, S. A. Clough, and W. D. Collins, 2008: Radiative forcing by long-lived greenhouse gases: Calculations with the AER radiative transfer models. *J. Geophys. Res.*, **113**, D13103, https://doi.org/10.1029/2008JD009944.

Janjić, Z. I., 1994: The step-mountain eta coordinate model: Further developments of the convection, viscous sublayer, and turbulence closure schemes. *Mon. Wea. Rev.*, **122**, 927–945, https://doi.org/10.1175/1520-0493(1994)122%3C0927:TSMECM%3E2.0.CO;2.

Jirak, I. L., and Coauthors, 2014: An overview of the 2014 NOAA Hazardous Weather Testbed Spring Forecasting Experiment. *27th Conf. on Severe Local Storms*, Madison, WI, Amer. Meteor. Soc., 46, https://ams.confex.com/ams/27SLS/webprogram/Manuscript/Paper254650/SLS2014_SFE2014_Overview_Ext_Abstract_Final.pdf.

Johnson, A., X. Wang, J. Carley, L. Wicker, and C. Karstens, 2015: A comparison of multiscale GSI-based EnKF and 3DVar data assimilation using radar and conventional observations for midlatitude convective-scale precipitation forecasts. *Mon.*

*Wea. Rev.*, **143**, 3087–3108, https://doi.org/10.1175/MWR-D-14-00345.1.

Jones, T. A., D. J. Stensrud, P. Minnis, and R. Palikonda, 2013a: Evaluation of a forward operator to assimilate cloud water path into WRF-DART. *Mon. Wea. Rev.*, **141**, 2272–2289, https://doi.org/10.1175/MWR-D-12-00238.1.

——, J. Otkin, D. J. Stensrud, and K. Knopfmeier, 2013b: Assimilation of satellite infrared radiances and Doppler radar observations during a cool season Observing System Simulation Experiment. *Mon. Wea. Rev.*, **141**, 3273–3299, https://doi.org/10.1175/MWR-D-12-00267.1.

——, ——, ——, and ——, 2014: Forecast evaluation of an Observing System Simulation Experiment assimilating both radar and satellite data. *Mon. Wea. Rev.*, **142**, 107–124, https://doi.org/10.1175/MWR-D-13-00151.1.

——, D. J. Stensrud, L. Wicker, P. Minnis, and R. Palikonda, 2015: Simultaneous radar and satellite data storm-scale assimilation using an ensemble Kalman filter approach for 24 May 2011. *Mon. Wea. Rev.*, **143**, 165–194, https://doi.org/10.1175/MWR-D-14-00180.1.

——, K. Knopfmeier, D. Wheatley, G. Creager, P. Minnis, and R. Palikonda, 2016: The NSSL Multiscale Ensemble. Part II: Combined radar and satellite data experiments. *Wea. Forecasting*, **31**, 297–327, https://doi.org/10.1175/WAF-D-15-0107.1.

Kleist, D. T., D. F. Parrish, J. C. Derber, R. Treadon, W.-S. Wu, and S. Lord, 2009: Introduction of the GSI into the NCEP Global Data Assimilation System. *Wea. Forecasting*, **24**, 1691–1705, https://doi.org/10.1175/2009WAF2222201.1.

Lei, L., J. L. Anderson, and J. S. Whitaker, 2016: Localizing the impact of satellite radiance observations using a global group ensemble filter. *J. Adv. Model. Earth Syst.*, **8**, 719–734, https://doi.org/10.1002/2016MS000627.

Lu, H., and Q. Xu, 2009: Trade-offs between measurement accuracy and resolutions in configuring phased-array radar velocity scans for ensemble-based storm-scale data assimilation. *J. Appl. Meteor. Climatol.*, **48**, 1230–1244, https://doi.org/10.1175/2008JAMC2009.1.

McNally, A. P., J. C. Derber, W. Wu, and B. B. Katz, 2000: The use of TOVS level-1b radiances in the NCEP SSI analysis system. *Quart. J. Roy. Meteor. Soc.*, **126**, 689–724, https://doi.org/10.1002/qj.49712656315.

——, P. D. Watts, J. A. Smith, R. Engelen, G. A. Kelly, J. N. Thépaut, and M. Matricardi, 2006: The assimilation of AIRS radiance data at ECMWF. *Quart. J. Roy. Meteor. Soc.*, **132**, 935–957, https://doi.org/10.1256/qj.04.171.

McPherson, R. A., and Coauthors, 2007: Statewide monitoring of the mesoscale environment: A technical update on the Oklahoma Mesonet. *J. Atmos. Oceanic Technol.*, **24**, 301–321, https://doi.org/10.1175/JTECH1976.1.

Menzel, W. P., and J. F. Purdom, 1994: Introducing GOES-I: The first of a new generation of Geostationary Operational Environmental Satellites. *Bull. Amer. Meteor. Soc.*, **75**, 757–782, https://doi.org/10.1175/1520-0477(1994)075<0757:IGITFO>2.0.CO;2.

Minnis, P., and Coauthors, 2011: CERES Edition-2 cloud property retrievals using TRMM VIRS and Terra and Aqua MODIS data—Part I: Algorithms. *IEEE Trans. Geosci. Remote Sens.*, **49**, 4374–4400, https://doi.org/10.1109/TGRS.2011.2144601.

Mlawer, E. J., S. J. Taubman, P. D. Brown, M. J. Iacono, and S. A. Clough, 1997: Radiative transfer for inhomogeneous atmospheres: RRTM, a validated correlated-k model for the longwave. *J. Geophys. Res.*, **102**, 16 663–16 682, https://doi.org/10.1029/97JD00237.

Nakanishi, M., and H. Niino, 2006: An improved Mellor–Yamada level-3 model: Its numerical stability and application to a regional prediction of advection fog. *Bound.-Layer Meteor.*, **119**, 397–407, https://doi.org/10.1007/s10546-005-9030-8.

Newman, J. F., V. Lakshmanan, P. L. Heinselman, M. B. Richman, and T. M. Smith, 2013: Range-correcting azimuthal shear in Doppler radar data. *Wea. Forecasting*, **28**, 194–211, https://doi.org/10.1175/WAF-D-11-00154.1.

Otkin, J., 2012a: Assimilation of water vapor sensitive infrared brightness temperature observations during a high impact weather event. *J. Geophys. Res.*, **117**, D19203, https://doi.org/10.1029/2012JD017568.

——, 2012b: Assessing the impact of the covariance localization radius when assimilating infrared brightness temperature observations using an ensemble Kalman filter. *Mon. Wea. Rev.*, **140**, 543–561, https://doi.org/10.1175/MWR-D-11-00084.1.

Polkinghorne, R., and T. Vukicevic, 2011: Data assimilation of cloud-affected radiances in a cloud-resolving model. *Mon. Wea. Rev.*, **139**, 755–773, https://doi.org/10.1175/2010MWR3360.1.

——, ——, and K. F. Evans, 2010: Validation of cloud-resolving model background data for cloud data assimilation. *Mon. Wea. Rev.*, **138**, 781–795, https://doi.org/10.1175/2009MWR3012.1.

Qin, Z., X. Zou, and F. Weng, 2013: Evaluating added benefits of assimilating GOES Imager radiance data in GSI for coastal QPFs. *Mon. Wea. Rev.*, **141**, 75–92, https://doi.org/10.1175/MWR-D-12-00079.1.

Ren, L. F., 2016: A case study of GOES-15 imager bias characterization with a numerical weather prediction model. *Front. Earth Sci.*, **10**, 409–418, https://doi.org/10.1007/s11707-016-0579-y.

Schmit, T. J., E. M. Prins, A. J. Schreiner, and J. J. Gurka, 2001: Introducing the GOES-M Imager. *Natl. Wea. Dig.*, **25**, 28–37.

——, M. M. Gunshor, W. P. Menzel, J. J. Gurka, J. Li, and A. S. Bachmeier, 2005: Introducing the next-generation Advanced Baseline Imager on GOES-R. *Bull. Amer. Meteor. Soc.*, **86**, 1079–1096, https://doi.org/10.1175/BAMS-86-8-1079.

Skamarock, W. C., and Coauthors, 2008: A description of the Advanced Research WRF version 3. NCAR Tech Note NCAR/TN-475+STR, 113 pp., https://doi.org/10.5065/D68S4MVH.

Skinner, P. S., L. J. Wicker, D. M. Wheatley, and K. H. Knopfmeier, 2016: Application of two spatial verification methods to ensemble forecasts of low-level rotation. *Wea. Forecasting*, **31**, 713–735, https://doi.org/10.1175/WAF-D-15-0129.1.

Smith, T. M., and Coauthors, 2016: Multi-Radar Multi-Sensor (MRMS) severe weather and aviation products: Initial operating capabilities. *Bull. Amer. Meteor. Soc.*, **97**, 1617–1630, https://doi.org/10.1175/BAMS-D-14-00173.1.

Stengel, M., P. Undén, M. Lindskog, P. Dahlgren, N. Gustafsson, and R. Bennartz, 2009: Assimilation of SEVERI infrared radiances with HIRLAM 4D-Var. *Quart. J. Roy. Meteor. Soc.*, **135**, 2100–2109, https://doi.org/10.1002/qj.501.

Stensrud, D. J., J.-W. Bao, and T. T. Warner, 2000: Using initial condition and model physics perturbations in short-range ensemble simulations of mesoscale convective systems. *Mon. Wea. Rev.*, **128**, 2077–2107, https://doi.org/10.1175/1520-0493(2000)128<2077:UICAMP>2.0.CO;2.

——, and Coauthors, 2009: Convective-scale warn-on-forecast system: A vision for 2020. *Bull. Amer. Meteor. Soc.*, **90**, 1487–1500, https://doi.org/10.1175/2009BAMS2795.1.

——, and Coauthors, 2013: Progress and challenges with warn-on-forecast. *Atmos. Res.*, **123**, 2–16, https://doi.org/10.1016/j.atmosres.2012.04.004.

Szyndel, M. D. E., J.-N. Thepaut, and G. Kelly, 2005: Evaluation of potential benefit of assimilation of SEVIRI water vapour

radiance data from Meteosat-8 into global numerical weather prediction analyses. *Atmos. Sci. Lett.*, **6**, 105–111, https://doi.org/10.1002/asl.98.

Thompson, G., R. M. Rasmussen, and K. Manning, 2004: Explicit forecasts of winter precipitation using an improved bulk microphysics scheme. Part I: Description and sensitivity analysis. *Mon. Wea. Rev.*, **132**, 519–542, https://doi.org/10.1175/1520-0493(2004)132<0519:EFOWPU>2.0.CO;2.

——, P. R. Field, R. M. Rasmussen, and W. R. Hall, 2008: Explicit forecasts of winter precipitation using an improved bulk microphysics scheme. Part II: Implementation of a new snow parameterization. *Mon. Wea. Rev.*, **136**, 5095–5115, https://doi.org/10.1175/2008MWR2387.1.

Vukicevic, T., M. Sengupta, A. S. Jones, and T. Vonder Haar, 2006: Cloud-resolving satellite data assimilation: Information content of IR window observations and uncertainties in estimation. *J. Atmos. Sci.*, **63**, 901–919, https://doi.org/10.1175/JAS3639.1.

Wang, Y., and X. Wang, 2017: Direct assimilation of radar reflectivity without tangent linear and adjoint of the nonlinear observation operator in GSI-based EnVar system: Methodology and experiment with the 8 May 2003 Oklahoma City tornadic supercell. *Mon. Wea. Rev.*, **145**, 1447–1471, https://doi.org/10.1175/MWR-D-16-0231.1.

Weng, F., 2007: Advances in radiative transfer modelling in support of satellite data assimilation. *J. Atmos. Sci.*, **64**, 3799–3807, https://doi.org/10.1175/2007JAS2112.1.

Wheatley, D. M., N. Yussouf, and D. J. Stensrud, 2014: Ensemble Kalman filter analyses and forecasts of a severe mesoscale convective system using different choices of microphysics schemes. *Mon. Wea. Rev.*, **142**, 3243–3263, https://doi.org/10.1175/MWR-D-13-00260.1.

——, K. H. Knopfmeier, T. A. Jones, and G. J. Creager, 2015: Storm-scale data assimilation and ensemble forecasting with the NSSL Experimental Warn-on-Forecast System. Part I: Radar data experiments. *Wea. Forecasting*, **30**, 1795–1817, https://doi.org/10.1175/WAF-D-15-0043.1.

Whitaker, J. S., T. M. Hamill, X. Wei, Y. Song, and Z. Toth, 2008: Ensemble data assimilation with the NCEP Global Forecast System. *Mon. Wea. Rev.*, **136**, 463–482, https://doi.org/10.1175/2007MWR2018.1.

Wilks, D. S., 2006: *Statistical Methods in the Atmospheric Sciences*. 2nd ed. International Geophysics Series, Vol. 100, Academic Press, 648 pp.

Wolff, J. K., M. Harrold, T. Fowler, J. H. Gotway, L. Nance, and B. G. Brown, 2014: Beyond the basics: Evaluating model-based precipitation forecasts using traditional, spatial, and object-based methods. *Wea. Forecasting*, **29**, 1451–1472, https://doi.org/10.1175/WAF-D-13-00135.1.

Wu, W., R. J. Purser, and D. F. Parrish, 2002: Three-dimensional variational analysis with spatially inhomogeneous covariances. *Mon. Wea. Rev.*, **130**, 2905–2916, https://doi.org/10.1175/1520-0493(2002)130<2905:TDVAWS>2.0.CO;2.

Yussouf, N., E. R. Mansell, L. J. Wicker, D. M. Wheatley, and D. J. Stensrud, 2013: The ensemble Kalman filter analyses and forecasts of the 8 May 2003 Oklahoma City tornadic supercell storm using single- and double-moment microphysics schemes. *Mon. Wea. Rev.*, **141**, 3388–3412, https://doi.org/10.1175/MWR-D-12-00237.1.

Zhang, F., M. Minamide, and E. E. Clothiaux, 2016: Potential impacts of assimilating all-sky infrared satellite radiance from GOES-R on convection-permitting analysis and prediction of tropical cyclones. *Geophys. Res. Lett.*, **43**, 2954–2963, https://doi.org/10.1002/2016GL068468.

Zhu, Y., J. Derber, A. Collard, D. Dee, R. Treadon, G. Gayno, and J. A. Jung, 2014: Enhanced radiance bias correction in the National Centers for Environmental Prediction's Gridpoint Statistical Interpolation data assimilation system. *Quart. J. Roy. Meteor. Soc.*, **140**, 1479–1492, https://doi.org/10.1002/qj.2233.

Zou, X., F. Weng, B. Zhang, L. Lin, Z. Qin, and V. Tallapragada, 2013: Impacts of assimilation of ATMS data in HWRF on track and intensity forecasts of 2012 four landfall hurricanes. *J. Geophys. Res. Atmos.*, **118**, 11 558–11 576, https://doi.org/10.1002/2013JD020405.

——, ——, V. Tallapragada, L. Lin, B. Zhang, C. Wu, and Z. Qin, 2015: Satellite data assimilation of upper-level sounding channels in HWRF with two different model tops. *J. Meteor. Res.*, **29**, 1–27, https://doi.org/10.1007/s13351-015-4108-9.